The Astrophysical Journal, 692:470–491, 2009 February 10 doi:10.1088/0004-637X/692/1/470

HIGH-VELOCITY CLOUDS IN THE NEARBY SPIRAL GALAXY M 83

Eric D. Miller[1], Joel N. Bregman[2], and Bart P. Wakker[3]
[1] Kavli Institute for Astrophysics and Space Research, Massachusetts Institute of Technology, Cambridge, MA 02139, USA; milleric@mit.edu
[2] Department of Astronomy, University of Michigan, Ann Arbor, MI 48105, USA
[3] Department of Astronomy, University of Wisconsin, Madison, WI 53706, USA
Received 2007 September 6; accepted 2008 October 24; published 2009 February 19

ABSTRACT

We present deep H I 21 cm and optical observations of the face-on spiral galaxy M 83 obtained as part of a project to search for high-velocity clouds (HVCs) in nearby galaxies. Anomalous-velocity neutral gas is detected toward M 83, with $5.6 \times 10^7\ M_\odot$ of H I contained in a disk rotating 40–50 km s^{-1} more slowly in projection than the bulk of the gas. We interpret this as a vertically extended thick disk of neutral material, containing 5.5% of the total H I within the central 8 kpc. Using an automated source detection algorithm to search for small-scale H I emission features, we find eight distinct, anomalous-velocity H I clouds with masses ranging from 7×10^5 to $1.5 \times 10^7 M_\odot$ and velocities differing by up to 200 km s^{-1} compared to the H I disk. Large on-disk structures are coincident with the optical spiral arms, while unresolved off-disk clouds contain no diffuse optical emission down to a limit of 27 r' mag per square arcsec. The diversity of the thick H I disk and larger clouds suggests the influence of multiple formation mechanisms, with a galactic fountain responsible for the slowly rotating disk and on-disk discrete clouds, and tidal effects responsible for off-disk cloud production. The mass and kinetic energy of the H I clouds are consistent with the mass exchange rate predicted by the galactic fountain model. If the HVC population in M 83 is similar to that in our own Galaxy, then the Galactic HVCs must be distributed within a radius of less than 25 kpc.

Key words: galaxies: individual (M 83) – galaxies: ISM – galaxies: kinematics and dynamics – radio lines: galaxies

Online-only material: color figures

1. INTRODUCTION

Our understanding of the gaseous content of our Galaxy has advanced greatly in recent years as instruments sensitive to a variety of wavebands have become available. One component of the Galaxy's gaseous neighborhood remains poorly understood: the ensemble of high-velocity clouds (HVCs). Initially discovered in 1963 by Muller et al. (1963), HVCs are clouds of H I gas that deviate in velocity from the differentially rotating disk of gas by 70–300 km s^{-1}. These structures have been studied extensively in H I emission, Hα emission, and absorption against background point sources, with several published catalogs detailing their observed characteristics (Wakker & van Woerden 1991, 1997; Wakker 2001; Putman et al. 2002).

A cursory inspection of the HVC catalogs reveals a tremendous variation in size, morphology, and velocity; this variation has led to a number of formation scenarios that predict different physical properties. One favored model is the Galactic fountain, a cyclic phenomenon whereby hot ($T \sim 10^6$ K) gas is ejected into the lower halo ($z \lesssim 10$ kpc) by supernova explosions (Shapiro & Field 1976; Bregman 1980). Here the gas cools and loses its buoyancy, free-falling back to the disk in sheets at mainly negative velocities approaching 100 km s^{-1}. A second scenario suggests accretion of close companion galaxies, either through tidal or ram-pressure stripping as a companion moves through the hot, extended Galactic halo. This is undoubtedly the origin of the Magellanic Stream (Mathewson et al. 1974), and there is recent evidence for gaseous remnants of satellite galaxies (Lockman 2003; Putman et al. 2004). Other scenarios propose alternate extragalactic origins, such as accreted intergalactic medium (IGM) material (Oort 1966, 1970, 1981) or discrete remnants of galaxy formation (Oort 1966; Blitz et al. 1999; Braun & Burton 1999). This last model attributes the most compact HVCs (CHVCs) to an ensemble of primordial, dark-matter-dominated "minihalos" streaming into the Local Group along filaments of moderate overdensity. Such clouds would have a typical distance of ~ 750 kpc, and total mass of $\sim 10^8$–$10^9\ M_\odot$ per cloud (assuming $M_{\rm H\,I} = 0.1 M_{\rm tot}$). Modeling by Sternberg et al. (2002) and simulations of CDM halo evolution by Klypin et al. (1999) and Moore et al. (1999) support a more local distribution of ~ 150 kpc. The clouds need not be dominated by dark matter, as uneven CDM halo cooling can result in fragmentation and produce a population of moderately ionized, pressure-confined clouds embedded in a hot corona (Maller & Bullock 2004).

One key discriminator between these production mechanisms is distance, yet this parameter is difficult to determine since HVCs contain no visible stars. The most direct method of searching for HVC absorption against background halo stars has met with limited success until very recently, yielding upper limits on the distances to five HVCs and eight intermediate-velocity clouds (IVCs; Wakker 2001). The upper bounds to the vertical z heights of these HVCs range from 0.2 kpc to 7 kpc, and the corresponding mass limits range from about 1 $M_\odot$ for a very small HVC to $2 \times 10^6\ M_\odot$ for Complex A. Recent work has placed stronger constraints on an additional four HVCs, placing them at distances of $\sim$ 5–15 kpc (Thom et al. 2006; Wakker et al. 2007, 2008). In particular, Wakker et al. (2008) infer a distance of 3.7–11.2 kpc for Complex C, suggesting an H I mass of $(3\text{–}14) \times 10^6\ M_\odot$.

Indirect methods have also been used to determine HVC distances, such as constraining the degree of ionization on the cloud surface. It is difficult to model the strength of the UV radiation field leaking out of the Milky Way, although there are indications that the field is sufficient to ionize at least the surfaces of an HVC (Bregman & Harrington 1986; Bland-Hawthorn &

Table 1
Predictions of HVC Production Scenarios

Scenario	Distance (kpc)	$\lvert v_{\rm dev}\rvert$ (km s^{-1})	Size (kpc)	$M_{\rm cloud}$ ($M_\odot$)	Z ($Z_\odot$)
IGM infall	<3	<150	<1	<10^4	0.1–0.3
Galactic fountain	<10	<150	<1	10^4–10^5	$\geqslant 1$
Companion stripping	5–100	<300	∼1	10^5–10^6	0.1–1
Circumgalactic warm clouds	∼150	<300	∼1	10^6–10^7	0.1–0.3
Circumgalactic DM halos	∼150	<300	∼1	10^6–10^7	0.1–0.3
Local Group DM halos	∼750	<300	1–10	10^8	0.1–0.3

Notes. Sizes and masses shown are typical values based on the median observed parameters of the HVC ensemble. Masses for the first three scenarios assume H I is the primary constituent of the cloud, while the others assume an neutral gas fraction of 0.1 (warm clouds) or H I to dark matter ratio of 0.1 (dark matter halos). Velocities for the Galactic fountain and IGM infall models assume an adiabatic corona of fully ionized gas with $T \sim 10^6$ K.

Maloney 1997). Several groups have identified ionized "skins" in a number of HVCs (Weiner & Williams 1996; Tufte et al. 1998; Bland-Hawthorn et al. 1998), and observations by Putman et al. (2003) of Hα emission in 25 HVCs limit their distances to $5 < z < 40$ kpc.

While recent progress has been made, large gaps remain in our understanding of Galactic HVCs, the nature of the gaseous Galactic halo, and the relationship between such a halo and the thin, star-forming disk. The various HVC production scenarios predict different consequences for galaxy formation and evolution. In Table 1, we outline the predictions of the scenarios described above in terms of observables (size, velocity) and physical properties (mass, metallicity). Our vantage point remains an impediment to discriminating between these scenarios, as we are embedded within the very medium we attempt to disentangle. The superposition of material in position and velocity complicates the analysis, and chance locations of statistically anomalous sources (such as the Magellanic Stream and large HVC complexes) bias the conclusions.

These problems are largely overcome by observing a large sample of external galaxies, constraining the fundamental properties of their diffuse halos, and extrapolating to the Milky Way. Until recently, extragalactic H I studies have concentrated on the structure of the kinematically cold disk, and the discovery of anomalous-velocity material has been serendipitous. Early evidence of anomalous H I appeared in the face-on galaxies M 101 (van der Hulst & Sancisi 1988; Kamphuis et al. 1991), NGC 628 (Kamphuis & Briggs 1992), and NGC 6946 (Kamphuis & Sancisi 1993), with detections of a few clouds of mass $M_{\rm H\,I} > 10^7\ M_\odot$. Integrated H I profiles from a sample of 14 face-on galaxies show evidence for high-velocity gas in 10 of the systems (Schulman et al. 1994). More recent observations of inclined galaxies have uncovered anomalous H I gas in every target imaged with sufficient depth. Deep radio synthesis observations of NGC 891 (Swaters et al. 1997; Oosterloo et al. 2007), NGC 2403 (Fraternali et al. 2002b), NGC 4559 (Barbieri et al. 2005), NGC 253 (Boomsma et al. 2005), and NGC 6946 (Boomsma et al. 2008) have revealed vertically extended, slowly rotating "thick" disks of H I, suggestive of Galactic fountain activity. Modeling of a subset of these data confirm this conclusion, although some amount of IGM infall is required to prevent escape of the fountain gas and to produce the gas kinematics that are observed (Fraternali & Binney 2008). A GBT study of M 31 has uncovered for the first time a population of discrete HVC-like H I clouds in an external galaxy (Thilker et al. 2004). These objects are all within 50 kpc of the galaxy. Surveys of galaxy groups have so far failed to detect HVC analogs without optical counterparts (e.g., Zwaan 2001; Pisano et al. 2007, and references therein). Extrapolation by Pisano et al. (2007) of results from six Local Group analogs suggest the Galactic HVCs all lie within 90 kpc of the Galaxy.

Table 2
M 83 Properties

NGC number	5236	Type[c]	SBc(s)II
R.A. (J2000)	13h37m00s.8	Inclination[d]	24°
Decl. (J2000)	−29°51′59″	Pos. angle[d]	225°
l	314.°6	D_{25}[b]	12.′9
b	32.°0		17 kpc
Distance[a]	4.5 Mpc	$R_{\rm Holm}$[e]	7.′9
$v_{\rm hel}$[b]	503–516 km s^{-1}		10 kpc
B[b]	8.2	Total mass[e]	1–5 × 10^{11} $M_\odot$
M_B	−20.1	HI mass[e]	6.1 × 10^9 $M_\odot$
A_V	0.22	1′	1.3 kpc

Notes.
[a] Karachentsev et al. (2002).
[b] de Vaucouleurs et al. (1991).
[c] Sandage & Tammann (1987).
[d] Talbot et al. (1979).
[e] Huchtmeier & Bohnenstengel (1981).

In this paper, we describe the first results of a search for HVCs in nearby external spiral galaxies. We concentrate on face-on galaxies, since the line-of-sight velocity of the rotating H I disk is minimized and the parameter space available for HVC searching is maximized. These targets provide a necessary complement to the numerous inclined spirals which have been recently observed, as detailed above. By combining the H I data with deep optical surface photometry, we can constrain the amount of starlight in any anomalous H I clouds we find.

The next section summarizes the observations and reduction of both the H I and broad-band optical data. In Section 3, we discuss features of the bulk H I and optical disks. In Section 4, the cold H I disk is modeled and subtracted, and extended anomalous H I emission is analyzed. Section 5 discusses the detection of discrete anomalous H I emission, introducing a new detection algorithm (further detailed in Appendix A) and presenting simulations that constrain the effectiveness of this technique. The discussion in Section 6 places our results in context of previous work and predictions. Our conclusions are summarized in Section 7.

2. OBSERVATIONS & DATA REDUCTION

M 83 is a nearby (4.5 Mpc; Karachentsev et al. 2002), face-on grand-design spiral galaxy located in the Centaurus A group. While the optical, star-forming disk is small and well defined (Talbot et al. 1979), the H I disk is very extended, reaching to 6.5 times the optical Holmberg radius with 80% of the total H I mass found outside this radius (Huchtmeier & Bohnenstengel 1981). The H I disk is resolved into distinct rings and arms in this region, exhibiting a high degree of warping (Tilanus & Allen 1993). The basic properties of M 83 are presented in Table 2.

2.1. H I 21 cm Data

The radio data for M 83 were obtained in three separate observations with the VLA[4] on 1999 February 24 and 28 and

[4] The VLA is operated by the National Radio Astronomy Observatory, a facility of the National Science Foundation operated under cooperative agreement by Associated Universities, Inc.

Table 3
VLA Configuration and Data Parameters

Dates of observation	24 Feb, 28 Feb, 1 Mar 1999	
Time on source	12.2 hr	
No. antennas	26	
Central freq.	1.418 GHz	
Primary beam HPBW	31′.2	
Synth. beam HPBW	37″.2 × 33″.1	
Synth. beam PA	−72°.5	
1σ noise (per 5.17 km s^{-1} chan.)	0.94 mJy/beam	
1σ HI col. density (per 5.17 km s^{-1} chan.)	4.6×10^{18} cm^{-2}	
1 mJy beam^{-1}	0.49 K	
	Raw Data	Processed/Cleaned
Bandwidth	3.125 MHz	2.56 MHz
	660 km s^{-1}	540 km s^{-1}
Velocity range	183–843 km s^{-1}	230–770 km s^{-1}
No. channels	256	105
Channel separation	2.58 km s^{-1}	5.17 km s^{-1}
Channel width	3.10 km s^{-1}	5.17 km s^{-1}

March 1. To match the beam size with the scale of the expected emitting regions (1 kpc = 46″ at 4.5 Mpc), we chose to observe in the DnC configuration, in which the northern arm of the array is in the more extended C configuration. For sources at southern declinations such as M 83 (meridian altitude = 26°.1 at the VLA's latitude of +34°.1), this configuration produces a more symmetric uv-plane coverage pattern and a synthesized beam of about 35″ FWHM (0.76 kpc at a distance of 4.5 Mpc). Each observing run consisted of a 5 minute observation of the primary flux calibrator 3C 286, with a scan integration time of 20 s. This was followed with a series of ∼ 50 minute exposures of M 83 with integration times of 60 s, intermixed with 5 minute exposures of the secondary calibrator 3C 283. The total time spent on source was 12.2 hr.

The VLA spectral line correlator was configured to observe in the 1420 MHz frequency band, or "*L*-band." The correlator configuration and resulting data parameters are summarized in Table 3. To allow detection of H I emission at highly anomalous velocities, we used the largest bandwidth offered by the correlator, 3.125 MHz. This corresponds to a velocity width of 660 km s^{-1}, of which only the inner 540 km s^{-1} were retained because of edge noise. With the bandwidth centered on the systemic velocity of M 83, this enabled detection of features deviating by ±270 km s^{-1} from systemic. We expected the features to have linewidths of ∼ 20–30 km s^{-1} FWHM, therefore a velocity resolution of 5–10 km s^{-1} would have been sufficient for this project. To make the dataset generally usable to the community, we chose to observe at the full spectral resolution, with no on-line Hanning smoothing applied, and using the single IF correlator mode (sensitive only to right-handed circular polarization). This resulted in 256 channels with a channel separation of 12.2 kHz (2.58 km s^{-1}) and a channel width of 14.6 kHz (3.10 km s^{-1}).

The uv calibrator data were edited in a standard iterative way, with the inner 75% of the bandpass combined and inspected for obviously bad samples. Once all anomalous samples were excised from the calibrator data, the frequency-independent calibration was applied to the object data, which were then edited. The calibration solutions had a maximum closure error of 1% in amplitude and 1° in phase. The (frequency-dependent) bandpass correction was applied using the secondary calibrator 3C 283 as reference, again following an iterative editing/calibrating method. Application of the bandpass correction produced closure errors of 0.5% in amplitude and 0°.5 in phase, however because of the limited integration time of the calibrator, the noise in the final data cube was increased by a factor of 1.8. With the editing and calibration completed, the uv data were Hanning smoothed in velocity space. Besides improving the signal-to-noise ratio (S/N) in individual channels, smoothing with a Hanning kernel reduced the number of channels from 256 to 128 and made them independent, with channel width and separation equal at a value of 24.4 kHz (5.17 km s^{-1}).

The ultimate success of any interferometry observation hinges on whether a reliable map of source intensity in real space can be produced from incomplete sampling of the coherence function in the uv plane. At the imaging stage, weighting visibilities based on their local population density or distance from the tracking center affects the strength of sidelobe structure. We applied two weighting schemes to improve the quality of the principal solution: first, the "robust" scheme developed by Briggs (1995) to produce a mixture of natural and uniform weighting with a single parameter; and second, a Gaussian taper function to downweight visibilities in the sparsely-sampled outer uv plane. We used the `AIPS IMAGR` task (Greisen 1998) and applied a variety of values for these two weighting schemes, empirically determining the best compromise between sidelobe structure, resolution and sensitivity. The best compromise among all the considerations was a ROBUST value of 0 and a Gaussian uv-taper with $r_{0.3} = 6$ kλ, where $r_{.3}$ is the half-width at 30% of maximum. This weighting scheme increased the noise in the final image by a factor of 1.2 compared to pure natural weighting and no uv-taper.

A dirty image cube was produced from the full uv dataset, and channels free of H I line emission were identified. The continuum was subtracted by fitting a first-order polynomial to 10 line-free channels on each edge of the band and subtracting this from all channels. A continuum-free dirty image cube was produced from this uv dataset, using a cell size of 7″ per pixel and only including the central 105 channels to eliminate edge noise.

To correct for incomplete sampling in the uv plane and reduce the level of the sidelobes, one typically uses the dirty image to iteratively construct a model of the true brightness distribution. This is the strategy behind the CLEAN algorithm (Högbom 1974; Clark 1980), under which the brightness distribution is modeled iteratively as a set of δ-function "clean components." CLEAN is very effective at removing sidelobes from point sources, since the clean components themselves are modeled as points. Spatially extended H I emission, however, is poorly modeled by a set of point sources. Furthermore, while the strength of extended emission is usually relatively weak compared to a continuum point source, and thus the sidelobes associated with a single grid point often fall below the noise in a dirty map, the summation of sidelobes due to complex extended structure can be significant and difficult to disentangle.

To combat this problem, another method of image deconvolution was developed by Wakker & Schwarz (1988). Their Multi-Resolution CLEAN (MRC) runs the CLEAN algorithm, but operates on the point-like and extended sources separately. First, the dirty map and beam are smoothed then subtracted from the original map and beam to obtain a full-resolution difference map and beam. Clean beams are constructed for the smooth and difference beams, and CLEAN is performed on the smooth and difference maps separately. By performing CLEAN on a smoothed map, two major improvements are made in reproducing extended emission: the clean beam is closer in

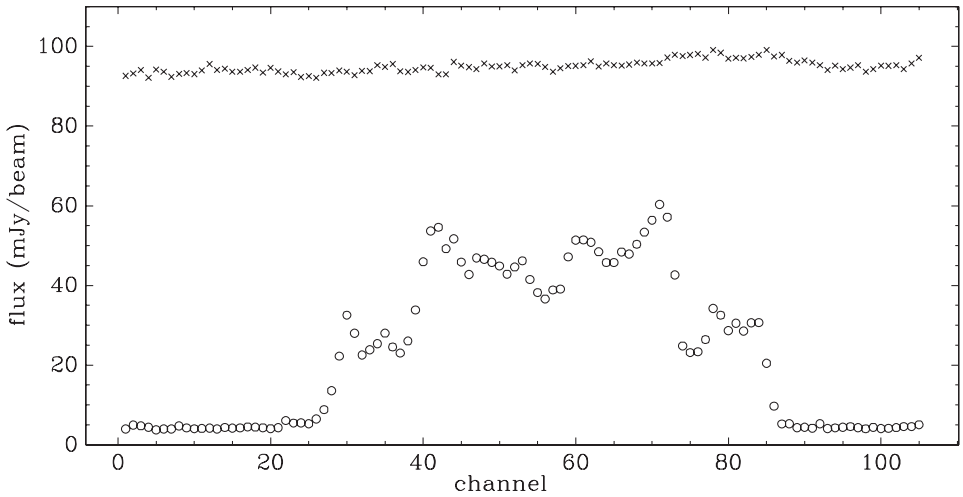

Figure 1. 1σ noise (crosses) and the peak H I flux (circles) in individual channels of the cleaned M 83 data cube. The noise levels have been multiplied by a factor of 100 and placed on the same scale as the peak flux to facilitate comparison. The noise is close to constant over the entire cube, with an rms of 1.7% and maximum variations less than 5% of the mean.

size to the extended sources one is attempting to model; and the signal-to-noise is improved, allowing detection of fainter sources. The original resolution is retained (and point sources are deconvolved) by cleaning the difference map separately and then combining the two resulting cleaned maps along with the full-resolution residuals. A detailed explanation of the method and the exact scaling parameters used are presented by Wakker & Schwarz (1988).

After trying standard CLEAN and MRC and comparing the results, it was determined that MRC was more effective in removing sidelobes. Our procedure was to clean the full region of each channel containing emission above the 3σ level, then examine the map for remaining strong sidelobes, which were present in most of the channels. The output cube was spatially smoothed to twice the beam size and binned up by five channels, and regions that contained significant emission were manually delineated with polygons. The cleaning was repeated with MRC, using the original dirty cube and allowing clean components only within the specified region of each channel. Successively deeper cleaning was performed, down to a threshold of 1σ.

The 1σ noise level, calculated from the emission-free regions of each image plane, and other parameters for the cleaned data cube are summarized in Table 3. The noise of 0.94 mJy/beam is larger than the theoretical value of 0.7 mJy/beam for this instrumental setup and image weighting parameters, and this is likely a result of the bandpass calibration. The noise is similar from channel to channel, varying no more than 5%, as is shown in Figure 1.

To reduce image size and ease further computational analysis, the image cube was binned 2 × 2 in space. With a final pixel size of 14″, the ∼ 35″ (FWHM) synthesized beam is still well sampled. Noise was not reduced, however, since neighboring pixels are correlated. The channel maps for the cleaned data cube are shown in Figure 2.

2.2. Optical Data

The optical data for M 83 were taken with the 0.6m Curtis Schmidt telescope located at Cerro Tololo Inter-American Observatory[5] (CTIO) in March 1999. Use of a thinned SITe 2K CCD chip resulted in a field of view of nearly 70′ with 2.″3 square pixels. To reduce flat-fielding errors that could be produced by nonrepeatable filter wheel positioning and dislodged dust particles, we used a single Sloan r' filter, keeping the filter wheel unchanged throughout the run. A standard observing scheme was followed, with twenty bias frames and six to eight twilight flats taken each evening, and standard star fields imaged at a range of airmass throughout the night. Approximately half of the telescope time was spent imaging galaxies and half imaging blank sky flats, with exposure times of 15 minutes each. The total exposure times were 10 hr on source and 8.75 hr on blank sky. Dark exposures taken during one cloudy night indicated no measurable CCD dark current.

The initial reduction procedure followed a standard formula. The bias and overscan were removed from all twilight, sky and object frames. A first-order flatfield was created for each night from the twilights flats. This flatfield was applied to the sky flats, which were co-added and smoothed with a 128 × 128 boxcar to remove stars. This sky correction image was normalized and multiplied by the first-order twilight flat field to produce a master flat field for each night, which was applied to the M 83 data. The individual galaxy frames were examined by eye, and eight of the 40 images contained undesirable features such as strong scattered light and were rejected. The remaining frames were sky-subtracted, aligned, and co-added. For proper noise estimation in future analysis, an average sky value of 4423 ADU was added back in to the co-added frame. Finally, the poorly-sampled outer regions were clipped, leaving a final 72′ × 69′ image with a total integration time of 8.0 hr.

Photometric calibration was accomplished with observations of standard stars. The number of standard stars for the Sloan filter system was limited at the time of observations, but using a star list provided by J.A. Smith (1999, private communication), we identified a number of standard stars within Landolt (1992) fields. Nightly imaging of these fields yielded 50 observations of seven standard stars covering a range of airmasses ($1.07 < \sec z < 2.0$) and colors ($0.0 < B - V < 1.0$). For a pixel size of 5.31 square arcsec and an effective exposure time of 900 s, the surface brightness corresponding to 1 ADU pix^{-1} in the final averaged galaxy frame was 30.11 ± 0.05 r' magnitudes per square arcsec. The average sky value of 4423 ADU corresponds to a surface brightness of 21.04 r' magnitudes per square arcsec, and the pixel-to-pixel noise in the final image (6.5 ADU)

[5] CTIO is part of the National Optical Astronomy Observatory, which is operated by the Association of Universities for Research in Astronomy (AURA), Inc., under cooperative agreement with the National Science Foundation.

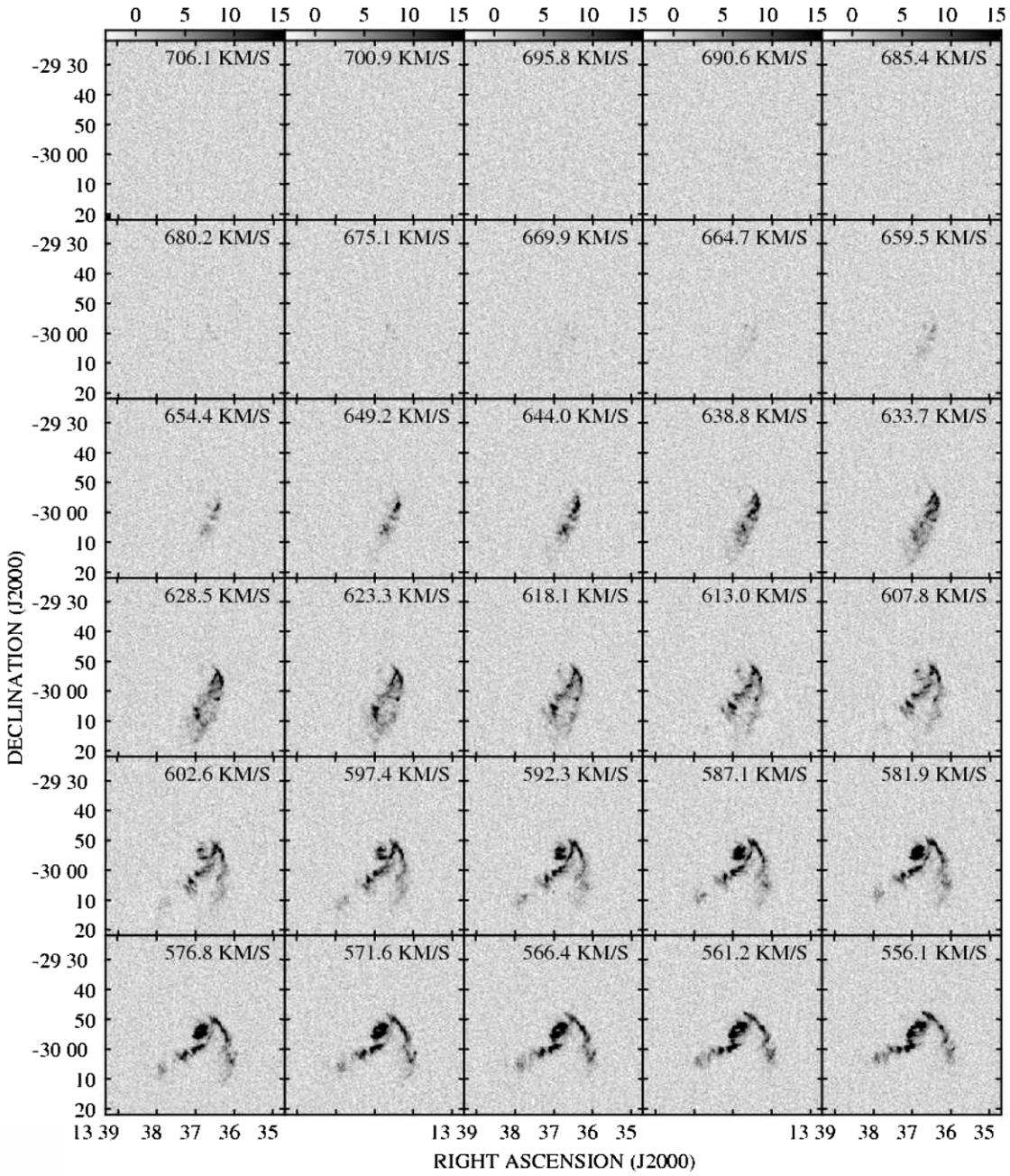

Figure 2. M 83 H I channel maps. Heliocentric velocities are marked in the upper right of each channel map. The grayscale ranges from −3 to 15 mJy to show the fainter structure in each channel, therefore most of the bright features appear saturated. Only channels with measurable H I emission are displayed.

corresponds to 28.1 r' magnitudes per square arcsec. Our 3σ limiting surface brightness is 26.9 r' magnitudes per square arcsec, not accounting for systematic errors caused by scattered light and large-scale flatfielding effects.

Foreground stars were removed by modeling the stellar point spread function (PSF) and masking each star. Using the DAOPHOT (Stetson 1987) package in IRAF,[6] we estimated the brightness of all stars in the frame by searching for 3σ peaks in the image and performing simple aperture photometry on them. This procedure produced 38,721 stellar objects; of these, 11 bright, isolated stars were chosen to construct the PSF. The PSF stars had an average (standardized) brightness of $r' = 16.3$, with one moderately saturated star included to improve the fit in the wings. The PSF was constructed from the unsaturated regions of the PSF stars, using an elliptical Moffat function with $\beta = 2.5$ as the analytic PSF component plus a single look-up table for the residual PSF component. The PSF was scaled to each PSF star and subtracted, leaving a residual image and revealing previously unidentified stars in the PSF stars' wings. These were fit with the PSF and removed from the original frame, and a new PSF was constructed. This procedure was iterated several times until the companion stars were completely removed and the PSF did not improve between iterations.

Once the PSF was modeled, it was used to identify and measure all stars in the field. Of the stars originally identified by aperture photometry, a subset of 33,950 were found to have

[6] IRAF is distributed by the National Optical Astronomy Observatories, which are operated by the Association of Universities for Research in Astronomy, Inc., under cooperative agreement with the National Science Foundation.

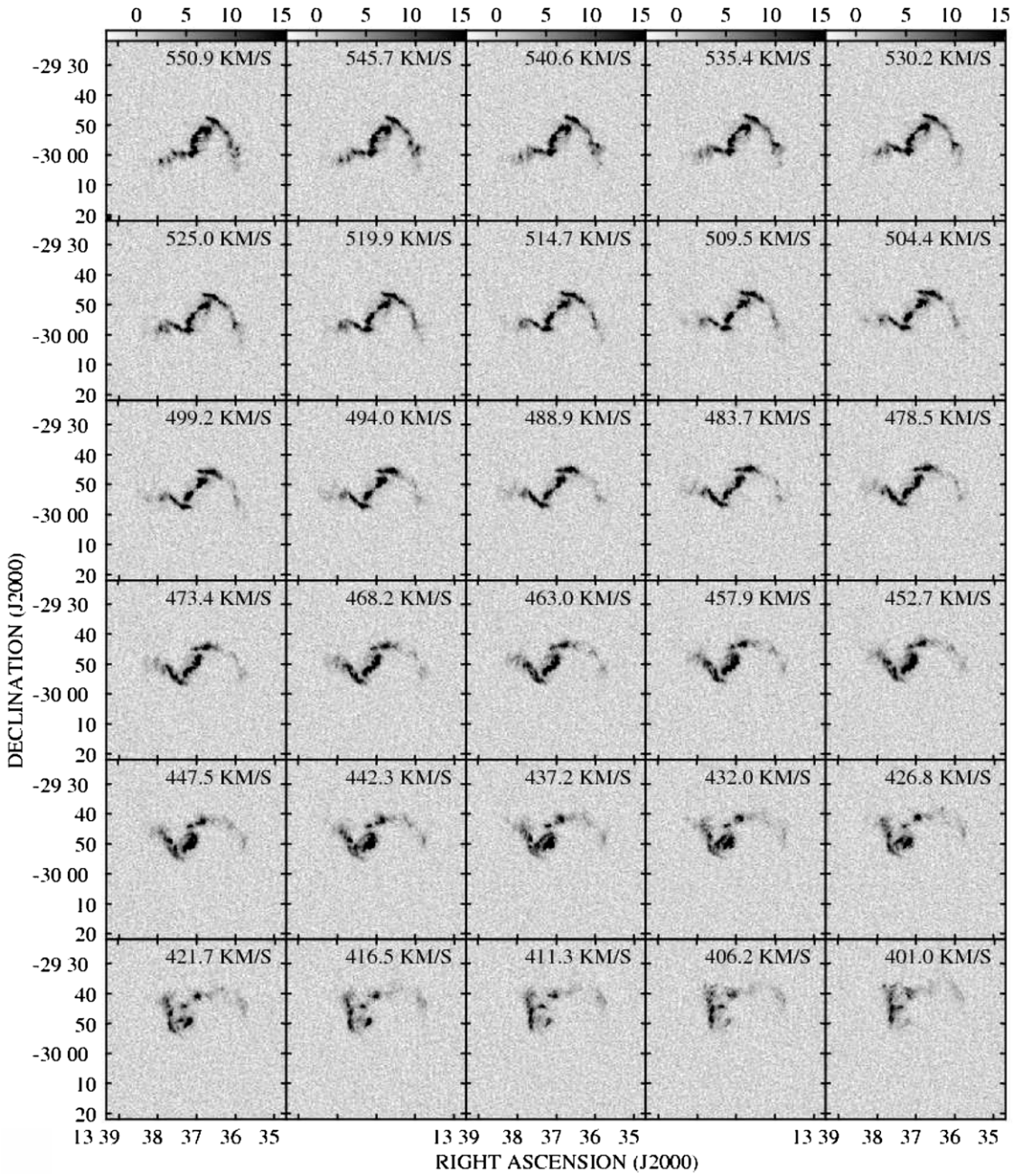

Figure 2. (Continued)

profiles similar to the PSF. This amounts to an average of 6.8 field stars per square arcmin, down to a detection limit of $r' = 23.8$. The core of a star becomes saturated at $r' \sim 14.5$, but by just fitting to the unsaturated wings, stars down to $r' \sim 11$ could be reliably measured.

Stars were removed by masking each one out to the radius at which its flux fell below a specified threshold. This method is a compromise between elimination of polluting starlight and retention of usable data. To construct the mask, the model PSF was averaged radially to a one-dimensional function, scaled to each star according to its magnitude, and used to determine the radius at which the stellar flux fell below threshold. A threshold of 2 ADU, well below the 7 ADU rms noise in the co-added frame, was a satisfactory compromise between starlight removal and pixel retention. Typical PSF reference stars were masked out to a radius of 7 pixels (16″), and the brightest unsaturated stars were masked out to a radius of 9 pixels (21″), about 26 times larger than the average seeing HWHM of about 0.″8.

Some contaminating features did not conform to the shape of the PSF and were ignored by the above procedure. These included background galaxies, very bright saturated stars, diffraction spikes, and charge transfer ("bleeding") features, and they were masked by hand.

3. THE NORMAL GALACTIC DISK OF M 83

3.1. H I Moment Map Construction

The bulk distribution and kinematics of emission-line gas are most easily summarized by moment maps, including the total H I surface brightness (0th moment) and the intensity-weighted mean velocity field (1st moment). To construct the moment maps, the image cube was first smoothed spatially to a round

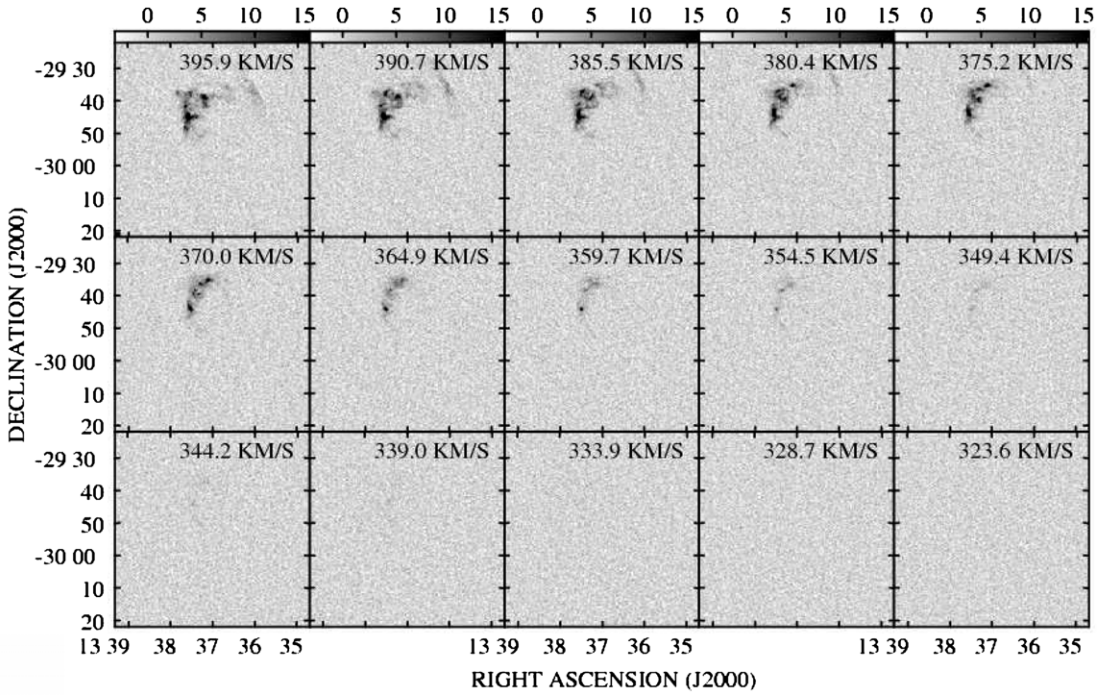

Figure 2. (Continued)

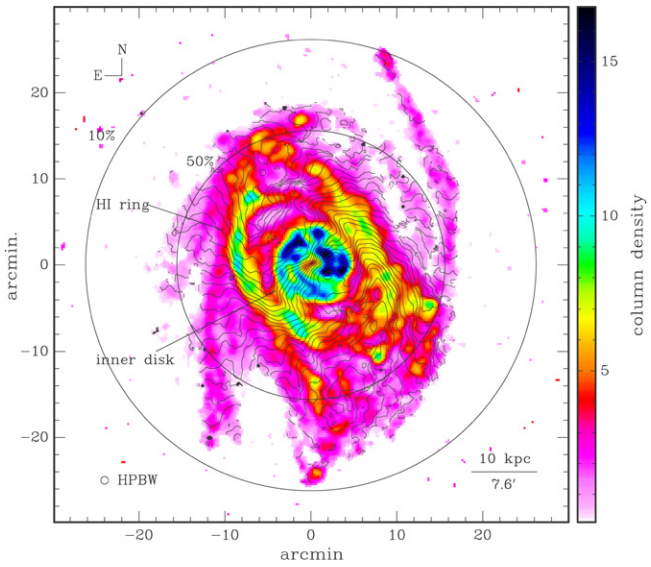

Figure 3. H I column density map for M 83. The inner circle shows the FWHM of the primary beam, while the outer circle shows the full width at 10% of peak sensitivity. Contours show the mean H I velocity and range from 350 to 650 km s^{-1} in steps of 10 km s^{-1} (twice the velocity resolution). Column density is in units of 10^{20} cm^{-2}. The marked features are discussed in Section 3.2.

(A color version of this figure is available in the online journal.)

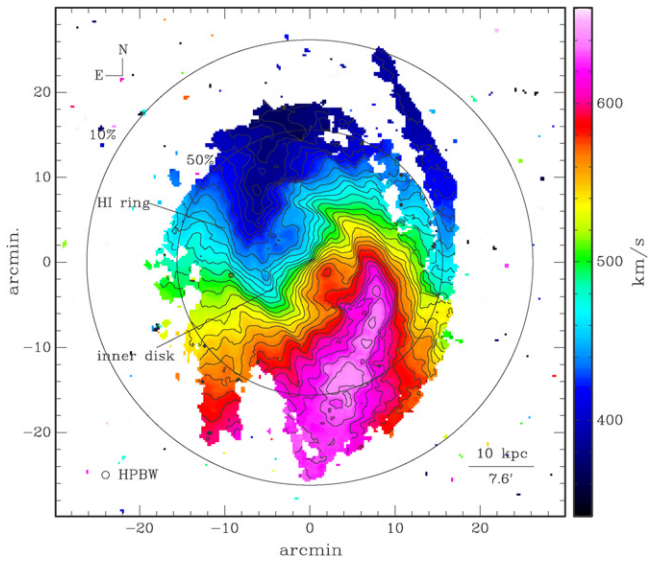

Figure 4. Intensity-weighted mean velocity map for M 83. Notations and contours are the same as in Figure 3, and velocities are heliocentric.

(A color version of this figure is available in the online journal.)

beam of 52″ FWHM, roughly 1.5 times the size of the original synthesized beam. This smoothing is done to improve the S/N and ensure that the faint extended components of emission peaks are included in the summation. Pixels with flux greater than 4σ were included in the summation, as were immediate neighbor pixels in both space and velocity.

The moment maps are shown in Figures 3 and 4. The primary beam attenuation correction was applied to only the moment 0 map (which is shown in column density units) after integrating in velocity. Throughout this work, all H I intensity maps displaying either integrated H I emission or H I column density have been corrected for the primary beam sensitivity.

The total H I mass determined from the H I surface brightness map is $4.7 \times 10^9\ M_\odot$. This is lower than the distance-corrected value of 6.1×10^9 obtained by Huchtmeier & Bohnenstengel (1981), who mapped the emission out to about twice the radius as the present study. Their single-dish scans were impervious to zero-spacing issues of interferometry and recovered all of the emission in the beam. Our result is therefore in reasonable agreement with their value.

3.2. *H I Disk Features*

The total H I map (Figure 3) is a good tracer of spatial morphology, and it shows a number of notable features. The inner disk of M 83 contains a minimum in the H I approximately 1′ (1.3 kpc) in diameter, with a measured column density of 4×10^{20} cm^{-2}. This feature is surrounded by the inner gaseous

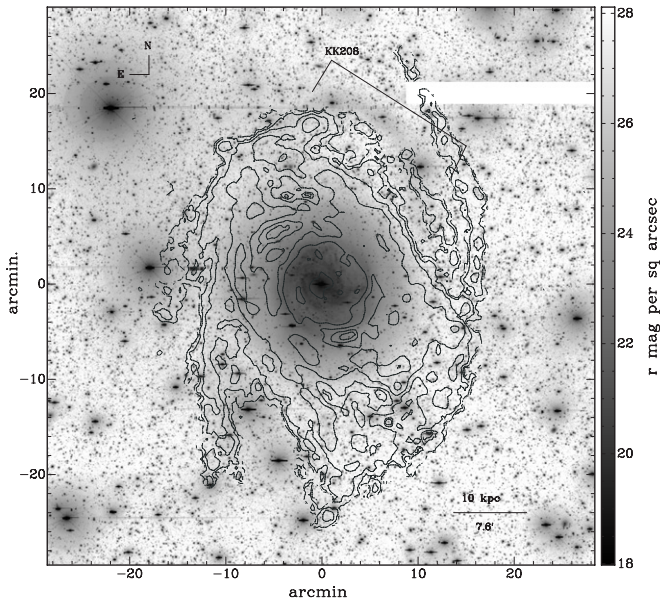

Figure 5. Optical image for M 83, displayed in linear units of r' magnitude per square arcsec. The contours show the column density of H I, starting at 5×10^{19} cm^{-2} and increasing by factors of 2. Also labeled is KK208, a faint companion galaxy or stellar stream to the northeast.

disk, which extends to a radius of 6′ (8 kpc) and ranges in column density from a minimum of 7×10^{20} cm^{-2} to a (probably optically thick) maximum of 1.7×10^{21} cm^{-2}. The inner disk shows a hint of spiral structure, with an irregular pattern of bright spots, and an aspect ratio close to unity, as one would expect for a nearly face-on galaxy. The small-scale structure is unresolved in our map, but it agrees qualitatively with the results of Tilanus & Allen (1993), who studied M 83 at higher spatial resolution.

Beyond 5′, the H I brightness falls off abruptly, with $N_{\rm H\,I} \lesssim 4 \times 10^{20}$ cm^{-2} in the region immediately around the inner disk. In the regions northeast and southwest of the inner disk, the column density becomes very low, approaching 5×10^{19} cm^{-2}. Further out, there is evidence of a bright ring of H I at a radius of 10′ (13 kpc). The ring has a peak column density of 1×10^{21} cm^{-2}, similar to the inner disk, and the projected thickness varies between 60″ and 80″. With the smoothed beam size (52″) this scale is unresolved, but the width can be no more than 1′ (1.3 kpc) after removal of the instrumental profile. The emission in the ring appears clumpy, with the brightest region in an arc on the west side of the galaxy. In addition, the aspect ratio of the ring is quite different from that of the inner disk, with semimajor and semiminor axes of 10′ and 5′ , respectively. The position angle is close to that of the inner disk (see below).

Outside of the ring, the H I spatial distribution becomes irregular, with arms and streams at various projected orientations. One arm appears just beyond the ring on the northwest side, and spans about 25′ (33 kpc) to a point 16′ (21 kpc) northeast of the disk center. There is a corresponding arm on the southeast to south side of the galaxy, at a similar projected distance. Two notable features are the arms further west of this, which extend from a common point 14′ (18 kpc) west of the center and extend toward the north. The longer of these arms reaches a projected galactic radius of 26′ (34 kpc) and is clearly detached from the rest of the disk. Both northwest arms appear to be mirrored in the southeast, and similar mirroring can be seen between other features and clumps in the extended H I. Since the primary antenna sensitivity falls to 10% of the central value for the most extended arms, these features could be even more extended than observed. It is clear that the arms are distinct from the main H I disk, down to our detection limit. The symmetrical nature and varying orientations of the outer arms indicates either a warp that varies with radius or a collection of kinematically distinct orbiting streams.

Analysis of the kinematic morphology can improve our understanding of the complex outer disk features, and this is most thoroughly done by combining the velocity field map, the individual channel maps, and the data cube as a whole. The velocity map is presented in both Figure 3 (as contours) and Figure 4 (as an image map and contours). In both figures, the inner disk shows a typical differential rotation pattern (a so-called "spider diagram"), with a central systemic value of $\sim$ 500 km s^{-1}. To estimate the systemic velocity and orientation, we fit the central 5′ with a Brandt rotation curve using the GAL task in AIPS (Greisen 1998). We find a systemic velocity of $v_{\rm hel} = 513 \pm 2$ km s^{-1}, where the error is estimated from the spread of best-fit values at different radii, and using the optical definition $v_{\rm hel,opt} = c(\lambda_{\rm obs} - \lambda_{\rm ref})/\lambda_{\rm ref}$. The best-fit position angle is 225° ± 2° (measured to the receding side from north to east), and the best-fit inclination is $i = 23° \pm 2°$.

Our estimates of the inner H I disk parameters are consistent with previous results. Previous values for the systemic velocity range from 505 km s^{-1} determined by Comte (1981) through Hα interferometry to 516 km s^{-1} quoted by de Vaucouleurs et al. (1991) and determined by H I observations. The HIPASS Bright Galaxy Catalog reports a value of 513 ± 2 km s^{-1} (Koribalski et al. 2004). We adopt 513 km s^{-1} as the systemic velocity for the remainder of this work. Our estimates of the orientation and inclination are consistent with the those quoted by Tilanus & Allen (1993), who have data with higher spatial resolution. Therefore we adopt $i = 22°$ for our inclination, and note that the maximum rotation rate of the inner disk is $v_{\rm rot,max} = (v_{\rm hel,max} - v_{\rm sys})/\sin i = 200$ km s^{-1}.

Outside of the inner disk, a discontinuity develops in the rotational velocity. This is most clearly seen in Figure 3, where the velocity contours bend abruptly into a warp, and in the channel maps for 440 km s^{-1} < $v_{\rm helio}$ < 540 km s^{-1} (see Figure 2). On the west side of the galaxy, the warp correlates well with the H I ring in projection, but on the east side the warp peaks inside of the ring. The isovelocity contours are shifted by 2′ counterclockwise from where they would be under ordinary differential galactic rotation. Beyond the ring, the isovelocity contours switch direction again, and they no longer reflect a flat rotation curve. In addition, the aspect ratio of the disk increases in this region, indicating that the axis of rotation is becoming more inclined to our line of sight as the radius increases. The highest radial velocities are seen near the very edge of the detected H I distribution, at a distance of 8′ (11 kpc) north and south of the galactic center.

It is apparent from this analysis that the inner disk, the ring, and the outer arms are kinematically distinct features. The ring and outer arms could be considered anomalous features themselves, however we wish to search for anomalous-velocity emission superposed on the bulk H I emission, and for this purpose we assume the outer arms are part of an extended disk of varying inclination.

3.3. Large-Scale Optical Features

The final optical image for M 83 shows many of the typical features of a face-on, grand-design spiral galaxy (see Figure 5). The spiral arms are seen radiating from a central bar-

like structure, and these arms contain a number of star clusters and dust lanes. The integrated H I intensity traces the spiral arms closely. The spiral structure is apparent only out to a radius of about 4.′5 (6 kpc) in the north and 5.′5 (7 kpc) in the south, at which point the surface brightness has dropped to 22.5 r' magnitudes per square arcsec. This is the same radius at which the inner H I disk falls off abruptly and at which the warp in the velocity field appears.

Beyond the inner optical disk, there is an extended optical envelope devoid of any structure. This envelope reaches a surface brightness of 26 r' mag per square arcsec at a radius of about 10′ (13 kpc), falling to undetectable levels at the location of the H I ring. In addition, the aspect ratio of the extended light, appearing stretched northeast to southwest, is different from that of the inner disk, which is nearly circular.

An arc-like feature can be seen projected 20′ (26 kpc) northwest of center, extending 12′ (16 kpc) northeast to southwest. This feature is barely visible in the Palomar Sky Survey plate covering this region, and it has been cataloged as a dwarf galaxy by Karachentseva & Karachentsev (1998), who designate it KK208. The surface brightness across the feature varies from 25–26 r' mag per square arcsec, although there are three bright stars along the arc that complicate masking and flux measurements. There is no measurable H I anywhere along the feature down to a 3σ column density limit of 1.5×10^{19} cm^{-2}. The arc lies between two outer H I arms, and it has a shape similar to those arms.

4. ANOMALOUS-VELOCITY H I: EXTENDED EMISSION

4.1. H I Disk Modeling

To search for anomalous-velocity material, one must first establish the criteria that make such material "anomalous." The difficulty of this can be appreciated by considering the ensemble of Galactic HVCs. A commonly-used definition limits membership to complexes with velocities deviating by greater than 100 km s^{-1} (or sometimes 90 km s^{-1}) relative to the Local Standard of Rest (LSR). This definition was intended to separate the HVCs from the so-called Intermediate Velocity Clouds (IVCs) and gas in the plane. However, such a definition does not take into account differential galactic rotation, an effect which can vary the observed velocity of a cloud by as much as 100 km s^{-1}, depending on the line of sight direction (Wakker 1991). To account for this effect, some authors have used the velocity relative to the so-called Galactic Standard of Rest (GSR), which is a point at the location of the Sun that does not participate in galactic rotation. This definition works well for gas at high $|z|$. However, it over corrects the velocity of any cloud that has a rotational component of motion, such as may be found closer to the plane. Wakker (1991) introduced the concept of "deviation velocity," which is the difference between the observed LSR velocity of the cloud and the maximum velocity expected along that line of sight due to differential rotation, assuming a simple model for the gaseous Galactic disk. At low latitudes in the Milky Way this varies greatly, but at latitudes above $\sim 40^\circ$ the velocity limit is around 60 km s^{-1}.

For external spiral galaxies, and especially face-on galaxies, the situation is simplified in that the bulk disk velocity is easily measured along any line of sight. Material at velocities different from this, assuming some velocity threshold or kinematic model for the disk, would be kinematically distinct from the cold H I disk and therefore anomalous. Hereafter we define anomalous-velocity material to be any H I emission that does not participate in the normal differential rotation of the bulk of H I along that line of sight. Implicit in the definition is the inclusion of spatially isolated H I clumps, since the disk rotation is undefined in regions where the disk does not exist. Therefore an anomalous-velocity clump (hereafter AVC or AV gas) can be anomalous in velocity or position.

As low-velocity AV gas could overlap and merge with the disk velocity, it is useful to remove any H I disk emission. Additionally, it is important to ignore this emission in a non-interactive source detection scheme. We modeled the disk of M 83 by fitting a Gaussian to the spectrum along every pixel of the cleaned image cube. The fitting was performed only along lines of sight where the peak exceeded 3.5σ (3.3 mJy/beam), and only included channels whose flux exceeded 1.7σ (1.6 mJy/beam). These criteria were applied to ensure that faint, velocity-broadened emission would not contaminate the thin disk fit.

Disk fitting and removal failed at warp discontinuities, where the H I disk has multiple velocity components across a scale of about 1′. It is not clear whether this spatial overlap of kinematically distinct disk components is a real feature or an effect of beam smearing, but in either case it poses a difficulty for effective disk removal. It is clear that the warp features are not AV material in our definition, since they define the disk velocity. We therefore attempted to remove this emission by refitting the original data cube with multiple Gaussian components. For lines-of-sight where the residual flux matched the above single-Gaussian criteria (i.e., peak above 3.5σ, 3 or more adjacent pixels with flux above 1.7σ), a two-component Gaussian was fit. The fitting threshold was kept high so that true AV gas would escape the fit.

To estimate the quality of the disk model, we examined the reduced χ^2 and covariance matrices of all the fits performed. The fits that included only a few data points were obviously poorly constrained, but inspection of the residual data cube showed that even these fits were reasonable. There were several lines-of-sight that had noticeably bad fits, but these were generally isolated pixels whose neighbors had similar parameters to each other. To remove the outliers, we performed a median box filtering on the fitting parameter images, using a kernel width of three pixels. The disk model and residual cube were reproduced from the adjusted fitting parameters, and inspection showed that the poor fits were removed and the disk subtraction was improved.

The fitted line-of-sight velocity dispersion varies across the galaxy, as can be seen in Figure 6. It reaches a maximum of 20 km s^{-1} in the center, averages about 15 km s^{-1} in the central H I disk and ring, and falls to 10 km s^{-1} or less in the extended disk and arms.

4.2. Extended, Disk-Like AV Gas

Removal of the H I disk results in a residual cube with significant H I emission remaining. For ease of display, we created position–velocity (p–v) plots, or slices through velocity along a line of specified location, length, and position angle. The slices were taken parallel to the major axis at a spacing of 70″ (twice the beamwidth). The value of a given pixel in the p–v image equals the distance-weighted average of the nearest four pixels in the channel. A sample of slices is shown in Figure 7 for both the full data cube and the residual.

Comparison of the slices with and without the disk emission clearly shows an emission component not well modeled by differential galactic rotation. This is especially evident along

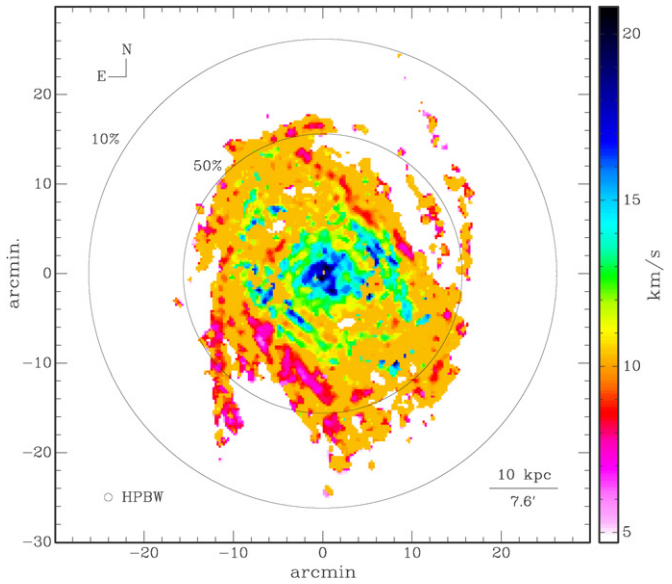

Figure 6. Line-of-sight H I velocity dispersion for M 83, obtained by fitting a Gaussian model to the disk emission. The fit was performed along every line of sight (pixel), but the values shown have been median box filtered to remove poor fits. The velocity dispersion is 20 km s^{-1} in the center, falling to less than 10 km s^{-1} in the outer regions.

(A color version of this figure is available in the online journal.)

the major axis. The anomalous component is spatially extended and clumpy, with deviation velocities generally ±40–50 km s^{-1} near the emission peak along any line of sight. The emission generally appears brighter on one velocity wing of the disk H I, toward the systemic galactic velocity.[7] Some of the anomalous emission occurs in the "forbidden" velocity region, which is the p–v quadrant on the opposite side of the systemic velocity from the disk. One interpretation is that material at velocities between the disk and galactic systemic would be rotating more slowly than the bulk of material in the galaxy. Material in the forbidden p–v region would be moving in the opposite sense of the bulk rotation along that line of sight, i.e., counter rotating. These interpretations assume the disk and anomalous material have similar spatial distribution and rotation axis orientation. In a face-on galaxy like M 83, material in the forbidden region is likely to be in vertical motion.

To quantify the amount of AV gas in M 83, we constructed column density and mean velocity maps from the residual cube (see Figure 8). The dynamical properties of the AV H I were determined from these maps and are summarized in Table 4. The mass of AV H I in the residual cube is 9.7 × 10^8 $M_\odot$, corresponding to 20% of the total H I. It was apparent that poor subtraction of the H I ring/warp and outer H I arms contaminated the residual cube, therefore we manually defined a region containing only anomalous emission projected on the central disk. The region used was an ellipse centered on the galaxy with a semimajor axis of 6.′0 (radius of 8 kpc), a semiminor axis of 4.′5, and a position angle of 45° as shown in Figures 8. This area contains the most dynamically homogeneous disk gas and produced reasonable model parameters. The total H I mass in this region, including the cold disk, is 1.02 × 10^9 $M_\odot$, of which 8.4 × 10^7$M_\odot$ or 8.2% is present in the anomalous

[7] Hereafter, velocities on the systemic side of the disk velocity will be referred to as "low relative velocity," while velocities on the opposite side of the disk velocity will be referred to as "high relative velocity." This designation places the velocities in the reference frame of the rotating galaxy.

Table 4
Extended AV Gas: Dynamical Properties

Component	F (Jy km s^{-1})	$M_{\rm H\,I}$ (10^7 $M_\odot$)	KE (10^{53} erg)
Full residual cube	203.0	97.0	21.0
Inner disk	17.6	8.4	16.0
Inner disk, low-v	11.8	5.6	8.7

component ("inner disk" in Table 4). The low-relative-velocity emission contributes 5.6 × 10^7 $M_\odot$ or 5.5% of the total inner disk H I.

The velocity field shows two high-velocity spots to the east and west of the galaxy center, identified by rectangles in Figure 8. These features are also seen on the high relative velocity side of the p–v slices, including one structure +1′ along the +140″ p–v diagram in Figure 7, at velocities between +50 and +100 km s^{-1}. In a simple model of disk rotation, these clumps would be rotating more quickly than the bulk of the H I. They are discrete in projection compared to the low relative velocity component described above, and will be discussed in detail in Section 5 (as AVCs 1 and 2).

Aside from these features, the motion and morphology of the residual emission mimic that of the galactic disk, with the southwest side receding and the northeast side approaching. The line-of-sight velocity dispersion ranges from 10–15 km s^{-1}, similar to the thin disk, although this may be an underestimate if the wings of the anomalous emission are excluded in the thin disk mask. A map of deviation velocity was produced by subtracting the velocity map of the modeled disk from that of the residual cube (see Figure 9), and it shows a rotation rate 40–50 km s^{-1} slower in projection. If the inclination of this disk of AV emission is also about 20°, then its rotation rate is about 100–150 km s^{-1}, compared to 200 km s^{-1} for the cold disk.

We used the deviation velocities to construct a map of the kinetic energy with respect to the cold disk (see Figure 9). Unlike the previous analysis, this interpretation assumes all motion is perpendicular to the galaxy plane,[8] and it provides an upper limit to the energy apportioned to vertical bulk motion. The total kinetic energy so derived is 2.1 × 10^{54} erg, with 1.6 × 10^{54} erg from gas within the inner disk and 8.7 × 10^{53} erg of that from the low-relative-velocity material. The last figure excludes discrete clumps, such as the one projected 2′ northwest of center; these features possess nearly half of the kinetic energy of the inner AV gas, and are fully discussed in Section 5. The 1.6 × 10^{54} erg from the inner 8 kpc is equivalent to the energy of 8 supernovae kpc^{-2}, although the z component of velocity is not known for this material, so this is an upper limit to the kinetic energy.

While the distribution of extended gas is well characterized by moment maps and p–v slices, faint, compact emission sources are easily overlooked. Detection of such systems requires a quantitative, objective searching technique that utilizes the entire set of data in a statistical way. The next section addresses our search for faint, discrete H I emission sources.

[8] Lacking any knowledge of transverse motion, we actually assumed motion fully along the line of sight, which is offset by 24° from the galactic pole direction. Thus velocities and kinetic energies are 10% and 20% lower, respectively, then what would be calculated for gas with only z-direction motion.

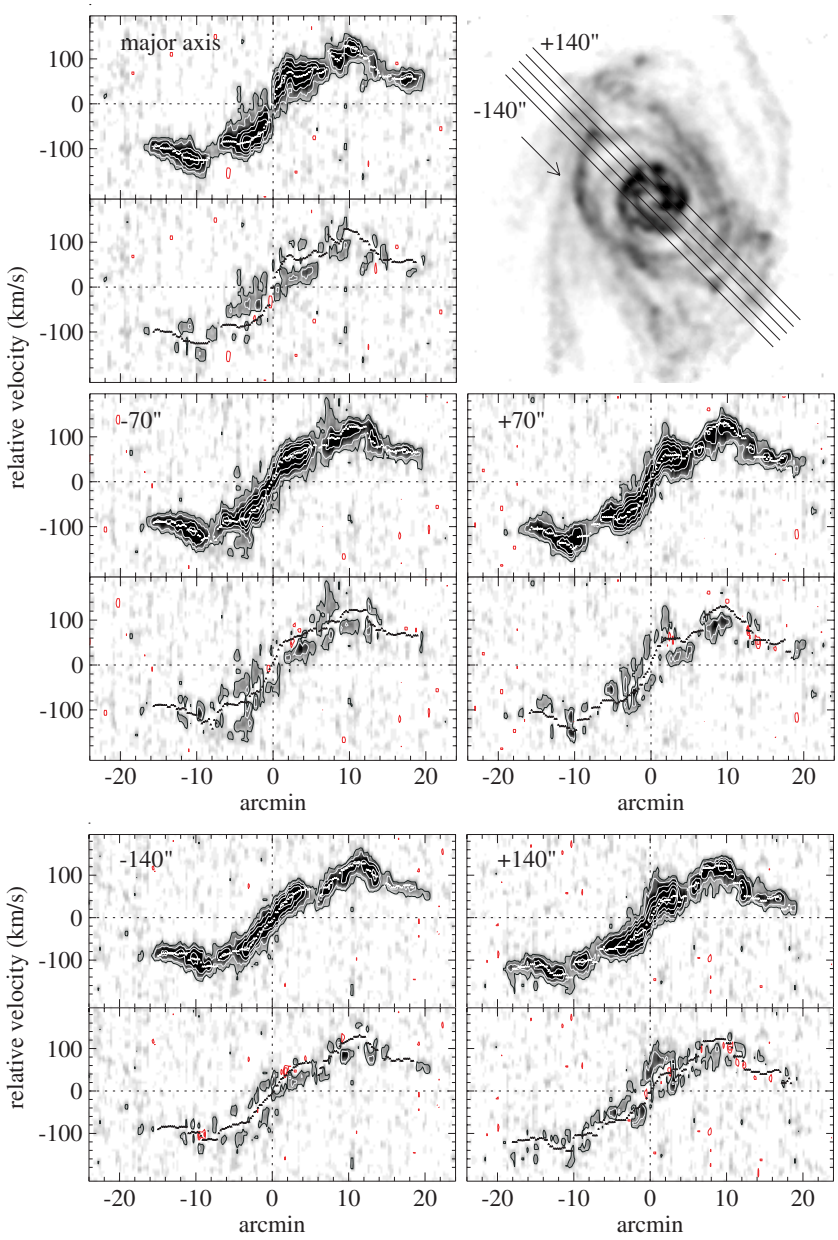

Figure 7. Position–velocity (p–v) diagrams for M 83, taken parallel to the major axis at separations of 70″, as plotted on the H I emission map (upper right) with the slice direction indicated by the arrow. Each slice, boxcar smoothed in velocity by three channels, is shown with the disk emission included (top) and subtracted (bottom). The rotation curve is traced by the white and black points. Grayscale ranges from 0 to 6 mJy beam^{-1}. Black and white contours begin at $+2\sigma$ and increase by factors of two. Red contours begin at -2σ and decrease by factors of two. Residual emission can be seen in all the slices, especially between the systemic and rotational velocity along the major axis.

(A color version of this figure is available in the online journal.)

5. ANOMALOUS-VELOCITY H I: DISCRETE EMISSION

5.1. Searching for AVCs

Compared to other observational subfields of astronomy, radio synthesis imaging suffers from a lack of robust, objective source detection software. Identifying sources and measuring their fluxes and other parameters is typically done by hand from moment maps and similar data products. For bright, point-like sources, this is not a problem, but difficulties arise when one wishes to search statistically for emission of unknown scale and location that may be projected on much stronger sources.

We have developed a suite of software that searches a three-dimensional data cube for signal in a statistical way. The software is described in detail in Appendix A and summarized here. The data cube is smoothed with a tunable velocity filter to emphasize sources of a particular velocity width, following the method of Uson et al. (1991). Peaks in this smoothed cube are identified and used to define three-dimensional "islands" of emission via contouring, using a variation of the CLUMPFIND algorithm developed by Williams et al. (1994). The velocity smoothing allows detection of kinematically broad but statistically significant features that might otherwise be overlooked. In addition, this algorithm allows a quantitative analysis of errors with the use of simulated datasets.

To search for discrete sources, we masked the residual H I cube within ± 20 km s^{-1} of the H I disk velocity to remove poorly-subtracted emission in the center of the disk profile. We ran the software with a peak threshold of 4σ, a clump

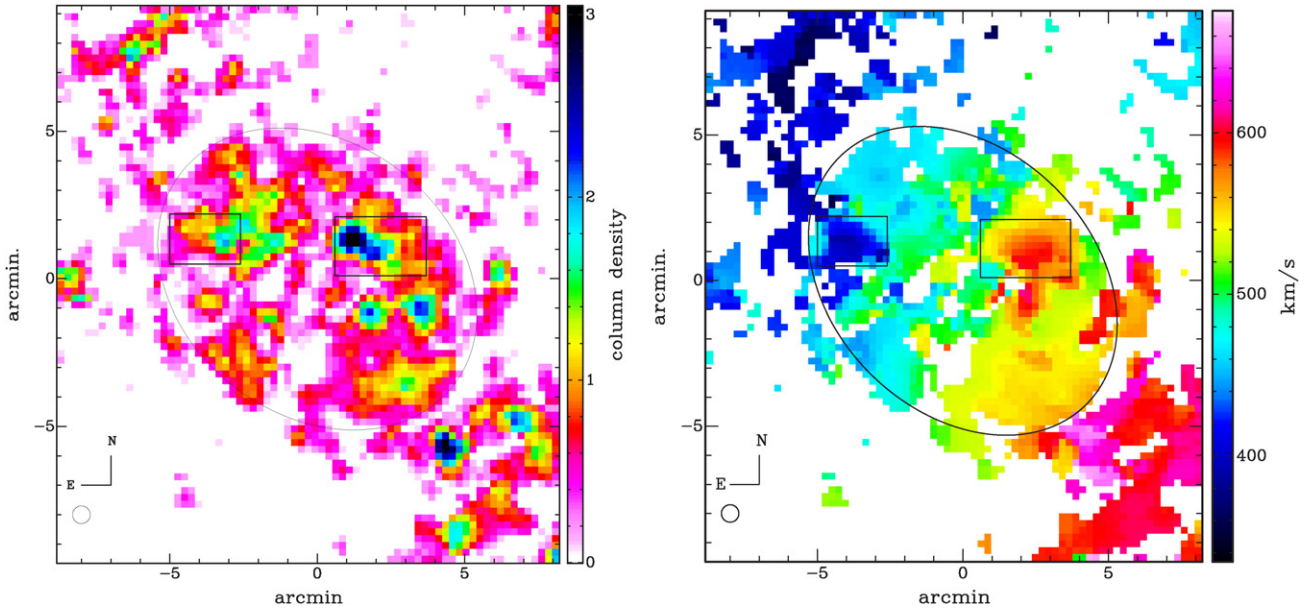

Figure 8. Maps of the AV emission in M 83, showing (left) column density (in units of 10^{20} cm^{-2}) and (right) mean velocity. The ellipse indicates the inner, well-modeled portion of the cold H I disk, and the rectangles identify discreet high-relative-velocity features, as described in the text. The anomalous gas appears disklike, rotating about 40–50 km s^{-1} more slowly in projection than the cold H I disk.

(A color version of this figure is available in the online journal.)

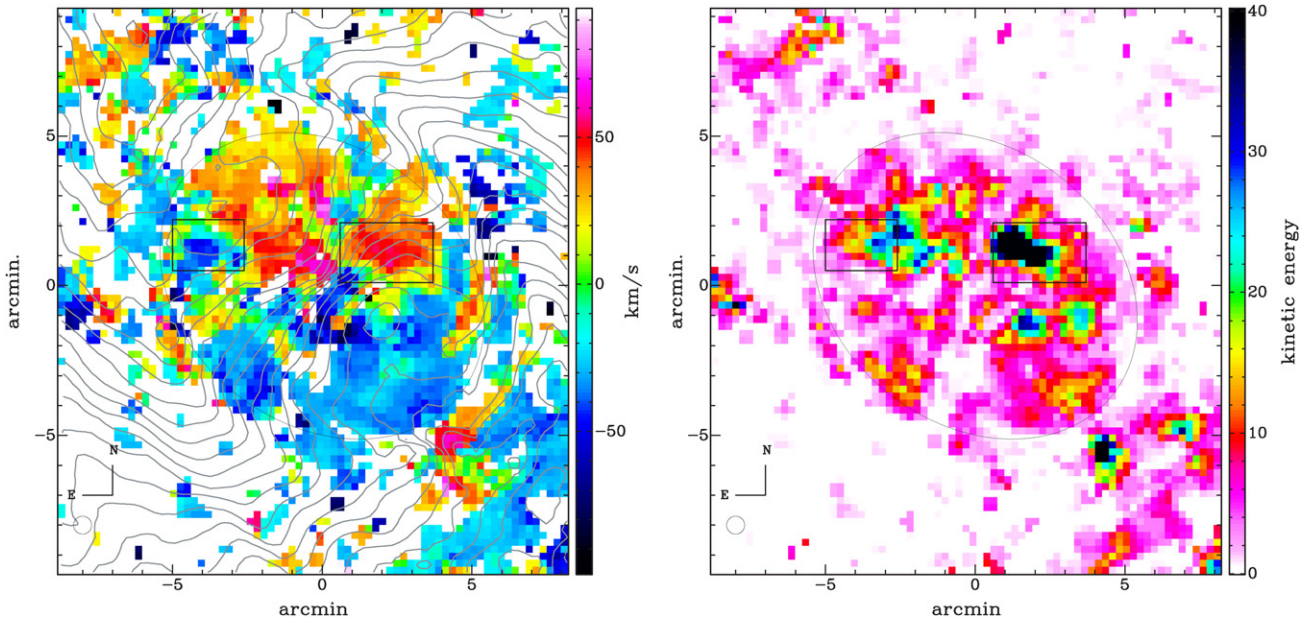

Figure 9. Maps of the AV emission in M 83, showing (left) deviation velocity and (right) kinetic energy per 14″ × 14″ pixel (in units of 10^{50} erg). The contours show the mean H I disk velocity in steps of 10 km s^{-1} for reference, and the other notations are as described in Figure 8. The anomalous gas appears disklike, rotating about 40–50 km s^{-1} more slowly in projection than the cold H I disk, but with about the same rotation axis. Most of the kinetic energy is contained in the feature 2′ northwest of center.

(A color version of this figure is available in the online journal.)

merging threshold of 2.5σ, and a clump extending threshold of 1σ. The width of the Gaussian filtering kernel was varied from 3–9 channels (15–45 km s^{-1}). For sources that were detected at multiple filter widths, we used the results from the filtering that produced the highest S/N (i.e., the kernel that was closest in width to the unsmoothed feature). The spatial and kinematic morphology of the candidate clouds was analyzed interactively using a variety of tools, including p–v plots, channel maps and three-dimensional visual rendering tools. A two-component Gaussian fit along the velocity axis at the clump centroid recovered the velocity and line width of the clump, as well as the line width of any H I disk emission along that line of sight. Finally, the flux of each clump was verified by hand using the standard radio method of aperture photometry. Values were consistent with the results from our automated software.

5.2. Detected Systems

We discovered 14 discrete clouds of H I emission at anomalous velocities or positions in the M 83 data cube. These AVCs are distinct from the bulk of the H I disk emission in that their contours of emission detach from the disk at levels approaching the map noise. The AVC properties are given in

Table 5
Discrete AVCs: General Properties

AVC[a]	R.A. (J2000)	Decl. (J2000)	v_{AVC}[b] (km s^{-1})	Ω[c] (sq. arcmin)	l[d] (′)	(kpc)	r_{proj}[e] (′)	(kpc)
1	13 36 49.2	−29 51 13	595 ± 2	2.63	5.3	6.9	1.7	2.2
2	13 37 19.3	−29 51 13	398 ± 2	2.75	5.5	7.2	3.7	4.8
3	13 36 42.7	−29 57 31	667 ± 2	0.77	2.8	3.6	7.1	9.3
4	13 37 18.3	−29 49 35	547 ± 2	0.58	2.5	3.3	4.4	5.7
5	13 37 12.9	−30 04 59	512 ± 2	0.39	1.7	2.2	13.4	17.4
6	13 37 08.6	−30 06 23	498 ± 3	0.39	1.8	2.3	14.6	19.0
7	13 37 06.4	−30 02 11	411 ± 2	0.39	1.5	2.0	10.0	13.0
8	13 36 56.8	−29 43 31	361 ± 2	0.39	1.9	2.5	8.4	11.0
9	13 37 33.4	−30 10 35	690 ± 8	0.39	1.3	1.7	19.9	25.8
10	13 38 11.8	−29 27 38	593 ± 5	0.39	1.2	1.6	28.6	37.2
11	13 37 21.6	−30 15 15	407 ± 12	0.39	1.6	2.1	23.9	31.1
12	13 35 45.7	−29 50 58	591 ± 5	0.39	1.0	1.3	16.5	21.5
13	13 37 25.9	−30 17 35	405 ± 5	0.39	1.4	1.8	25.9	33.7
14	13 35 19.0	−29 37 39	633 ± 32	0.39	1.2	1.6	26.3	34.2

Notes.
[a] AVCs 1–8 are considered real detections, AVCs 9–14 are likely spurious.
[b] Heliocentric radial velocity of the peak of the AVC emission.
[c] Solid angle subtended by the AVC after collapsing its HI emission along the velocity axis. A value of 0.39 sq. arcmin indicates the feature is unresolved.
[d] Greatest linear extent of the AVC, uncorrected for broadening by the synthesized beamwidth.
[e] Projected distance from the galactic center.

Table 6
Discrete AVCs: Dynamical Properties

AVC[a]	F_{meas}[b] (Jy km s^{-1})	F_{corr}[c] (Jy km s^{-1})	M_{HI}[d] ($10^6 M_\odot$)	N_{HI}[e] (10^{20} cm^{-2})	v_{dev}[f] (km s^{-1})	Δv[g] (km s^{-1})	KE[h] (10^{53} erg)
1	3.08 ± 0.07	3.12 ± 0.08	14.9 ± 0.4	2.9	+51	29 ± 2	3.9 ± 0.1
2	1.42 ± 0.06	1.48 ± 0.06	7.1 ± 0.3	1.4	−41	28 ± 2	1.2 ± 0.0
3	0.99 ± 0.05	1.12 ± 0.05	5.4 ± 0.3	2.6	+74	56 ± 4	2.9 ± 0.1
4	0.23 ± 0.03	0.24 ± 0.03	1.2 ± 0.1	0.6	+113	32 ±2	1.5 ± 0.2
5	0.11 ± 0.02	0.18 ± 0.04	0.8 ± 0.2	1.0	−77	15 ± 2	0.5 ± 0.1
6	0.11 ± 0.02	0.21 ± 0.04	1.0 ± 0.2	1.1	−103	15 ± 2	1.0 ± 0.2
7	0.13 ± 0.02	0.17 ± 0.03	0.8 ± 0.2	1.2	−166	44 ± 3	2.3 ± 0.4
8	0.11 ± 0.02	0.13 ± 0.03	0.6 ± 0.1	0.7	−90	24 ± 2	0.5 ± 0.1
9	0.08 ± 0.02	0.24 ± 0.06	1.2 ± 0.3	2.3	...	30 ± 2	...
10	0.14 ± 0.03	2.77 ± 0.52	13.2 ± 2.5	29.1	...	24 ± 2	...
11	0.19 ± 0.03	1.09 ± 0.17	5.2 ± 0.8	9.2	...	82 ± 5	...
12	0.06 ± 0.02	0.14 ± 0.04	0.7 ± 0.2	1.3	+135	29 ± 2	1.2 ± 0.3
13	0.16 ± 0.03	1.51 ± 0.27	7.2 ± 1.3	13.5	...	20 ± 2	...
14	0.15 ± 0.03	1.68 ± 0.31	8.0 ± 1.5	17.4	...	164 ± 12	...

Notes.
[a] AVCs 1–8 are considered real detections, AVCs 9–14 are likely spurious.
[b] Total flux in the AVC, uncorrected for the primary beam attenuation. Errors are 1σ.
[c] Total flux in the AVC, corrected for the primary beam attenuation.
[d] Mass of HI contained in the AVC.
[e] Peak column density of HI, integrated across the velocity width of the emission.
[f] Deviation velocity of the AVC, defined as the difference between the radial velocity of the peak AVC emission and the velocity fitted to the HI disk (if detectable) at that location, as described in Section 5.1.
[g] Full width at half maximum of a Gaussian fit to the velocity profile.
[h] Kinetic energy of the AVC found from the deviation velocity and mass. This is a lower limit to the total kinetic energy as only radial velocities are used.

Tables 5 and 6. The locations of the AVCs are shown superposed on the H I column density map in Figure 10 and superposed on the velocity map in Figure 11.

The AVCs are found across the H I disk of M 83, but they do exhibit a small degree of clustering, and several are located in regions where the kinematics of the disk are most complicated. Three clumps (1, 2, and 4) are located within the kinematically "normal" inner disk. One clump (3) is found at the inner disk/warp interface, two additional sources (7 and 8) are projected just beyond the ring, and four clumps (5, 6, 9, and 12) are found projected near outer H I arms. The remaining four AVCs (10, 11, 13, 14) are located well away from the center of the galaxy, at projected radii where the primary beam sensitivity falls to 10% or lower.

Gaussian fits and p–v plots were produced as described in the previous section, and these are shown for each AVC in Figure 12. The integrated H I intensity maps for the spatially-extended AVCs are shown in Figure 13. To eliminate the

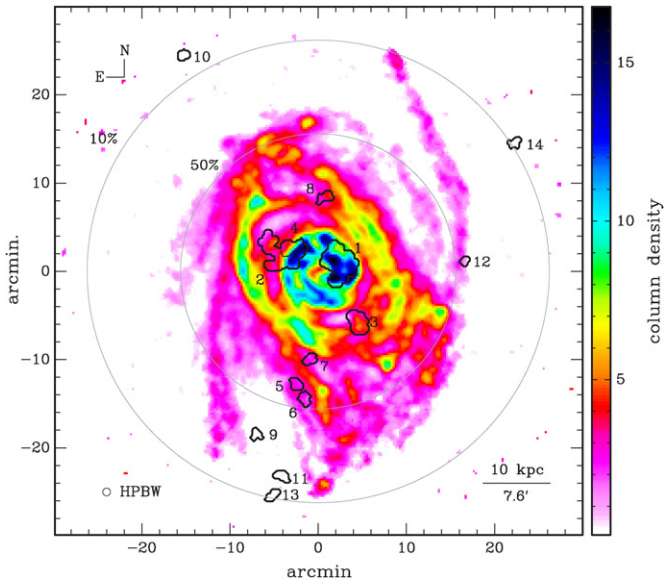

Figure 10. H I column density map for M 83, showing the locations of the detected AVCs. The shapes indicate the projected spatial extent of each AVC out to 1σ in H I column density (5×10^{18} cm^{-2}). The large gray circles indicate the primary beam sensitivity. The column density is in units of 10^{20} cm^{-2}.

(A color version of this figure is available in the online journal.)

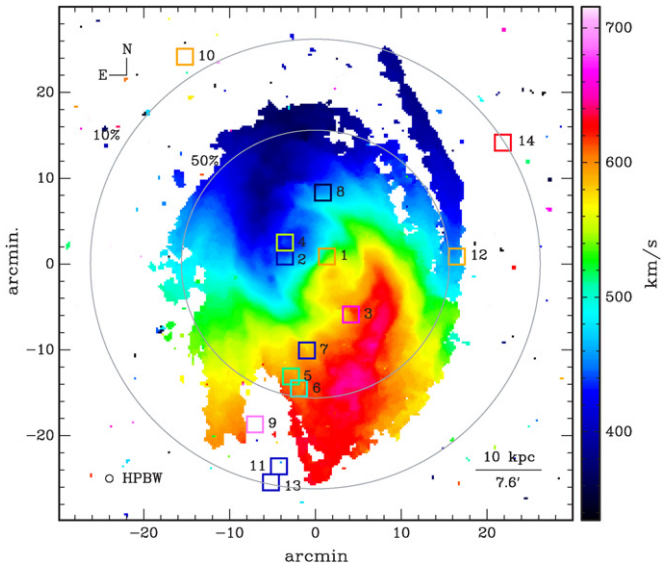

Figure 11. H I intensity-weighted mean velocity map for M 83, showing the locations of the detected AVCs. Each square is centered at the centroid of the AVC, with the color indicating its heliocentric radial velocity.

(A color version of this figure is available in the online journal.)

confusion of spatially varying noise, the p–v slices and intensity maps have not been corrected for the primary beam attenuation. The fluxes, masses, and column densities reported in Table 6 have been corrected for this effect.

A number of the AVCs have fluxes or velocity structure in the p–v plots that suggest they are spurious. From a "by-eye" analysis, we estimate that eight of these features (AVCs 1–8) are real detections and the remainder are not. Below we describe specific properties of individual AVCs, grouping them according to similar distribution and attributes. For completeness, we include features thought to be spurious, although these are excluded in our discussion in Section 6.

AVC 1. This source is the brightest and most massive AVC detected, with $M = 1.5 \times 10^7\ M_\odot$. Centered 2 kpc from the dynamical center of M 83, AVC 1 is also the only discrete clump projected over the inner H I disk. The intensity map and p–v plots show that it is spatially resolved and extended in velocity, with a deviation velocity $v_{\rm dev} = 51$ km s^{-1} and line width of 29 km s^{-1} FWHM. The measured line width is likely only accurate near the emission peak, as the p–v slices display a connection in velocity to the underlying disk emission. The projected intensity map supports this idea, with a secondary maximum projecting to the south, where the cold disk approaches the velocity of the cloud. The characteristics of this AVC are consistent with material flowing into or out of the disk, although the lack of spatial information along the line of sight complicates conclusions about the source's z height.

The moment and dynamical maps described in Section 4.2 clearly show emission from this feature (see Figures 8 and 9). The peak of the emission can be seen 1.′5 west and 1.′5 north of center in Figure 8(a).

AVCs 2, 4. These two clumps are close together in projection at a radius of about 5 kpc (near the edge of the inner disk), yet they differ greatly in their other characteristics. AVC 2 is bright, massive ($M = 7 \times 10^6\ M_\odot$) and extended ($\Omega = 2.8$ sq. arcmin, $l = 7$ kpc), while AVC 4 is less massive ($M = 1 \times 10^6\ M_\odot$) and barely resolved (largest linear extent $l = 3.3$ kpc). In addition, the deviation velocities of these clumps are quite different, with AVC 2 at high relative velocity ($v_{\rm dev} = -41$km s^{-1}) and AVC 4 at low relative velocity ($v_{\rm dev} = 113$ km s^{-1}). The line widths are similar, but the emission of AVC 2 appears to blend with the disk velocity. Emission from AVC 4 also blends kinematically with the disk, but the peak is more clearly separated, as can be seen in the velocity profiles in Figure 12. The heliocentric velocity of AVC 4 (522 km s^{-1}) places it in the "forbidden" region of counter-rotating material in the p–v plane. The spatial coincidence of these clumps hints at a correlation between them, possibly in the form of an expanding bubble (e.g., Kamphuis et al. 1991), but it is difficult to reconcile their differing morphological and kinematic structure. As with AVC 1, these two clumps appear in the AV gas maps shown in Figures 8 and 9.

AVC 3. At a projected distance of 9 kpc from the galactic center, this AVC appears in a region where the H I ring is disturbed and has a relatively low column density of $N_{\rm H\,I} = 3 \times 10^{20}$ cm^{-2}. The clump is extended in space, covering two synthesized beams in area and spanning 3.6 kpc. It is also extended in velocity, with a line width of 56 km s^{-1} FWHM, and its emission appears to merge with the disk H I at lower velocities. The source is massive ($M = 5.4 \times 10^6\ M_\odot$) and has a large kinetic energy of 3×10^{53} erg.

Although the clump is projected on a region of changing inclination between the inner disk and outer arms, it does not appear to result from beam smearing of a warp discontinuity. First, it is a compact structure, whereas a warp feature would be extended like the H I ring or outer arms. Second, it is much broader in velocity than the kinematically cold H I elsewhere in the galaxy. Finally, the kinematics of the surrounding disk material are regular in comparison to that seen at warp interfaces in other regions of the galaxy. This cloud is the only such feature seen along the H I ring.

This AVC appears at a location of low disk $N_{\rm H\,I}$. The p–v plots and Figure 10 show a lack of emission in the disk a few arcmin to the east of this location, although H I disk emission is present at the projected location of AVC 3.

AVCs 5, 6. These two AVCs have similar mass, size, line width, and deviation velocity. At a projected radius of about

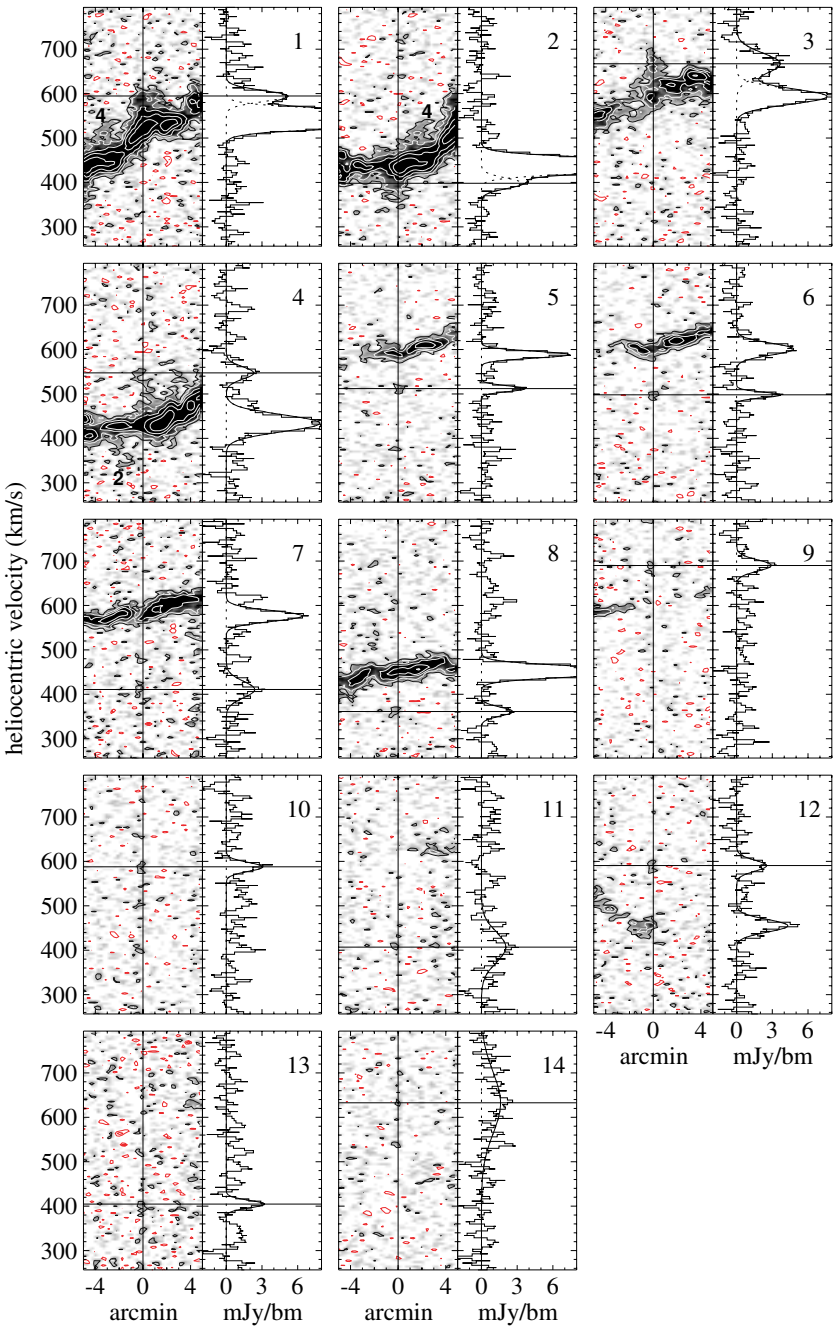

Figure 12. Position–velocity slices taken along the east–west direction and velocity profiles are shown for each AVC, which is centered at the intersection of the solid lines in the p–v plot. Grayscale ranges from 0 to 6 mJy beam^{-1}. Black and white contours begin at 2σ ($\sigma = 0.94$ mJy beam^{-1}) and increase by factors of two. Red contours begin at -2σ and decrease by factors of two. The profile plot, taken at the centroid of the AVC total H I emission, shows the Gaussian velocity fit to the AVC and H I disk (if present). AVCs which show up in multiple slices are identified by small numerals.

(A color version of this figure is available in the online journal.)

14′ (18 kpc) to the south of the galactic center, AVCs 5 and 6 are separated by 2′ (2.6 kpc) in projected space and 20 km s^{-1} in velocity. AVC 6 is the more massive and kinematically anomalous clump, with a mass of $1 \times 10^6\ M_\odot$ and deviation velocity of -103 km s^{-1}. AVC 5 has a mass of $8 \times 10^5\ M_\odot$ and deviation velocity of -77 km s^{-1}. The line width of both clumps is 15 km s^{-1}, producing a velocity dispersion of 6 km s^{-1}. Unlike the previously discussed AVCs, the emission from these H I clumps does not merge with that of the disk in position or velocity.

In addition to similar kinematics, these two clouds have similar sizes and are spatially unresolved by the VLA synthesized beam. The FWHM of a Gaussian fit across either feature is 45″; when deconvolved from the ∼ 35″ synthesized beam, this implies a maximum source size of 30″ (∼ 0.7 kpc). Their similar characteristics and location hint at a possible relation, and they might be bright spots in a single H I feature, although this speculation is made less likely by the 20 km s^{-1} difference in deviation velocity and the small radial velocity dispersions.

AVCs 7, 8. These emission sources are similar in that they appear between the H I ring and an outer arm, although they are projected on opposite sides of center. Both have highly negative deviation velocities ($v_{\rm dev} = -166$ and -90 km s^{-1}),

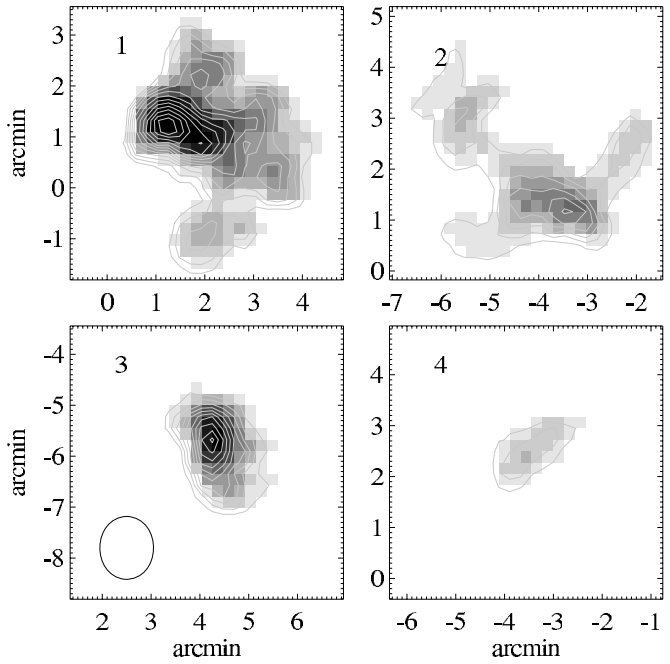

Figure 13. Integrated H I intensity maps for the four spatially extended AVCs. AVCs 1 and 2 have bright cores and low-level extended features, while AVCs 3 and 4 are more compact and only mildly resolved. Grayscale ranges from 0–0.25 Jy beam^{-1} km s^{-1}, and the contours are spaced at 0.025 Jy beam^{-1} km s^{-1}. The ellipse in the AVC 3 plot shows the HPBW of the synthesized beam. Coordinates are with respect to the center of M 83, with N up and east to the left.

are spatially unresolved, and have similar fluxes and masses ($M = 8$ and 6×10^5 $M_\odot$). Clump 7 has a large fraction of the kinetic energy of the AVC ensemble, due primarily to its large deviation velocity. From the integrated H I maps, which have the same colormap scale, one can see that AVC 7 is more sharply peaked than AVC 8. Consideration of the p–v plots and velocity profiles shows that the line of sight to AVC 7 contains emission at a variety of other velocities (e.g., −100, −40, +40 km s^{-1}). The clumps producing this emission fall below our threshold for clump identification, and it is unclear whether they result from real velocity structure in the AVC or from a systematic problem such as poor continuum subtraction or bandpass calibration.

AVCs 9, 12. Two clumps lie superposed on or near H I arms outside the half power width of the primary beam. Both are spatially unresolved and have similar line widths of 30 km s^{-1} FWHM. At these radii, the primary beam attenuation correction factor is about 3, so although both have small measured fluxes, the corrected masses are significant (1.1 and 0.6×10^6 $M_\odot$). Both AVCs have high deviation velocities, with $v_{\rm dev}$ = +135 km s^{-1} for clump 12, and a velocity difference of +100 km s^{-1} for clump 9 measured from the H I arm projected nearby. These detections are the least statistically significant of the set (4σ and 3σ for AVC 9 and 12, respectively), and they are hereafter treated as spurious.

AVCs 10, 11, 13, 14. All four of these clumps are in low-sensitivity regions, where the attenuation correction factor approaches 10. AVCs 11 and 13 are projected close together in space (2′ apart) and velocity (2 km s^{-1} apart). All four have strongly peaked emission maps, and their lines of sight contain emission at velocities throughout the data cube. In addition, AVCs 11 and 14 have very large line widths compared to the other AVCs. It is likely that these AVCs are not real, but are the result of systematic effects such as calibration errors. If they are real, the beam correction produces large masses and kinetic energies for these clumps.

Table 7
Optical Counterparts to H I AVCs

AVC[a]	$\mu_{r',0}$[b]	$\mu_{r',\rm lim}$[c]	Notes[d]
1	20.4	···	Inner disk, spiral arm
2	20.7	···	Inner disk, spiral arm
3	24.2	···	Inner disk
4	22.2	···	Inner disk
5	27.8	27.2	Stars
6	27.9	27.4	Stars
7	25.4	27.1	Stars
8	24.4	26.4	Outer disk, stars
9	26.5	27.0	Outer disk, stars
10	26.8	27.3	Stars, galaxy 1.5′ SE
11	27.2	26.8	Stars
12	27.5	26.8	Bright coincident stars
13	28.1	27.4	Stars
14	27.7	26.9	Stars, galaxy

Notes.
[a] AVCs 1–8 are considered real detections, AVCs 9–14 are likely spurious.
[b] The median surface brightness, in r' magnitudes per square arcsec, at the location of the AVC. For extended AVCs, the median was taken within the HPBW centered on the peak HI emission.
[c] The 3σ surface brightness limit on any optical features coincident with the AVC. This was determined by fitting and subtracting a plane from the optical image at that point. See that text for details.
[d] The notes identify optical features coincident with the AVC, including foreground stars, extended emission from M 83 (designated by location in the disk), and background galaxies.

5.3. Optical Counterparts to the AVCs

Searching for optical counterparts to the H I AVCs was carried out by hand. Each AVC was overlaid on the unmasked optical image, which was inspected for optical emission (see Figure 14). To search for small-scale emission structure superposed on the extended galaxy profile, the masked optical image was median filtered with a 5×5 pixel box. The location of each AVC was fit with a plane, excluding the four AVCs within the inner disk, which is difficult to fit with a simple model. The fit residuals were inspected for signal above the noise, which was not found in any case. The noise in the residuals was used to estimate surface brightness upper limits for optical counterparts. The results are shown in Table 7.

Below we describe possible counterparts and limits to the optical surface brightness for the individual AVCs. We discuss these limits in the context of other deep optical studies in Section 6.2.

AVCs 1, 2, 3, 4, 7, 8. These AVCS are all projected over the bright optical disk. The bright cores of AVCs 1 and 2 are projected on spiral arms, appearing to trace the shape of the arms, although this is possibly due to the method used to detect and delineate the H I clumps. The optical light coincident with AVC 1 peaks at 20.4 r' mag per square arcsec, excluding the bright star clusters in the spiral arms, and falls off to 22.1 r' mag per square arcsec in the outer part of the clump. Likewise, the core of AVC 2 is projected on a bright spiral arm, with $\mu_{r'} = 20.7$ r' mag per square arcsec. The optical light falls to 24.5 r' mag per square arcsec in the outer regions of this extended H I clump. While these AVCs align with spiral arms that contain star clusters, the spatial resolution of the H I data is insufficient to draw direct comparisons between AVC and star cluster morphology.

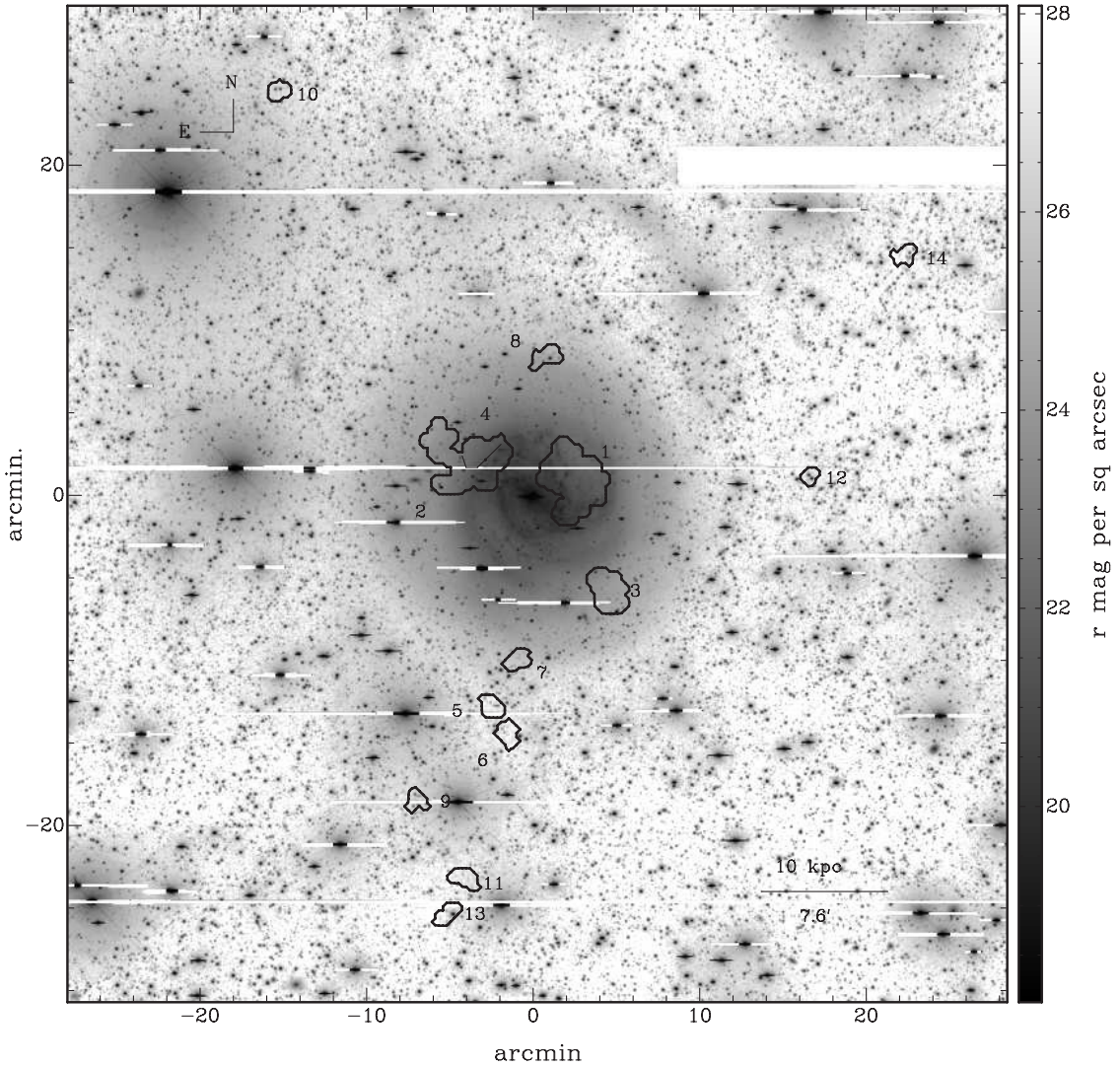

Figure 14. Optical M 83 image overlaid with the locations of the H I AVCs.

The other two AVCs within the inner disk, AVCs 3 and 4, have no obvious small-scale optical counterparts aside from stars. The inner edge of AVC 4 coincides with the outer edge of a spiral arm, although this is again likely due to the searching and masking technique we have employed. AVC 3 is projected on a disruption in the H I disk, but no evidence of such a feature is seen in the optical data.

Clumps 7 and 8 are projected further out, over the S and N edge of the extended stellar envelope. The underlying surface brightnesses in these regions is 25.4 and 24.4 r' mag per square arcsec, respectively. There are no small-scale optical features, aside from stars, down to the detection limit of about 27 r' mag per square arcsec.

AVCs 5, 6, 9, 11, 13. The majority of the large-radius AVCs contain only stars within the lowest H I contour. Clumps 5 and 6 are isolated from bright stars, but AVCs 9, 11, and 13 lie in the wings of very bright stars. As a result, much of the light in these regions is masked out to determine the surface brightness, and the amount of flux below a limiting magnitude of about 26 r' mag per square arcsec is poorly constrained. There is no evidence for emission down to this level, however.

AVCs 10, 12, 14. These three AVCs are positioned on or near optical features that could be related. AVC 10 is projected 1.′5 northwest of an object with a galactic light profile. The contours of AVC 14 contain a similar object. Both objects are smaller than the extent of the AVCs, although the H I clumps are unresolved. Given their apparent size, it is likely that these optical sources are background galaxies, although it is impossible to verify without spectroscopic data.

Clump 12 is centered on the location of two bright stars, making the limiting magnitude at this location difficult to determine. There is no signal at this position in the 1.4 GHz continuum map, therefore it is unlikely that the detected H I results from poor continuum subtraction. It is more likely that this is a chance superposition between bright stars and a detected H I source (real or spurious).

5.4. AVC Detection Simulations

To analyze our results quantitatively, it is necessary to determine the significance of the detections in terms of the completeness and false detection rate. Interferometry maps differ from images made with non-interferometric devices in that neighboring spatial pixels are not independent. The transformation of limited samples from the uv plane to the image plane results in the signal from every location being spatially smeared. Resolution elements therefore overlap each other, and more importantly, noise features are extended and often similar

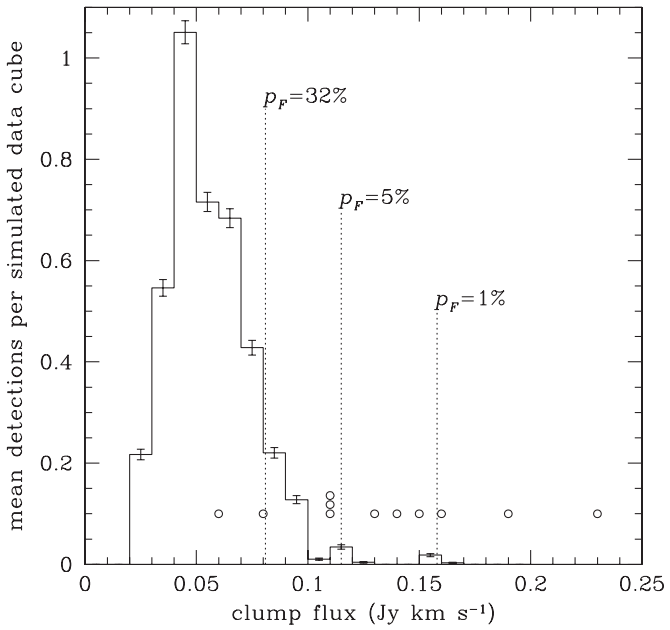

Figure 15. Flux distribution of false detections in the simulated pure noise data cubes. The binned values have been scaled to equal the mean number of false detections per masked M 83 data cube per 0.01 Jy km s^{-1} flux bin, so that the integral of this distribution equals the mean expected number of false detections in our data cube, a value of 4.1. The dotted lines note the likelihood p_F of obtaining at least one false detection above the given flux value in a single data cube (see the text for further explanation). Open circles indicate the fluxes of detected clumps in the M 83 data, with the three brightest clumps (AVCs 1–3) excluded. For clump flux > 0.1 Jy km s^{-1}, there is an excess over purely spurious detections.

in size to the objects being searched for. Prior to primary beam correction, the noise is nearly constant across the field. It is upon this background of spatially-dependent fluctuations that one searches for discrete emission features.

To investigate the sensitivity of our data, we simulated 2000 observations of Gaussian noise in the uv plane, using the same uv distribution and noise characteristics as our filtered M 83 observations. Each dataset was transformed to the image plane using the same technique described in Section 2.1, so that the resultant image cube had dimensions, spatial coherence (i.e., synthesized beamwidth) and σ identical to that of the cleaned, binned M 83 data cube. Each simulated cube was processed with our detection software, using identical parameters as described in Section 5.1, except for a single filtering kernel of five channels (25 km s^{-1}) FWHM, the average linewidth of the AVCs. The histogram of clump flux values, scaled to the parameter space volume of a single masked M 83 data cube, is shown in Figure 15. The low-flux side of the histogram shows a rapid fall-off due to decreasing detection efficiency. The histogram peaks near 0.045 Jy km s^{-1}, which is about 4.5 times the 1σ flux for a single beam in the smoothed cube (see Appendix A). This is consistent with our detection threshold of 4σ.

We can use the simulated distribution to calculate the likelihood of obtaining at least one spurious detection above a given flux threshold in the data cube. If we assume the false detection rate is determined by Poisson statistics, we find that the likelihood of obtaining at least one detection above flux F is given by $p_F = 1 - e^{-\mu_F}\mu_F^{\nu}/\nu! = 1 - e^{-\mu_F}$ for $\nu = 0$. The mean expected number of detections μ is given by the integral of the empirical distribution between F and $+\infty$, and it is a straightforward matter to find F for various values of p_F. The flux limits for $p_F = 0.32$, 0.05, and 0.01 are plotted in Figure 15. Several of our AVCs have fluxes (uncorrected for attenuation) within the region of nonzero false detection rate. If we exclude the three significant clumps with uncorrected fluxes near or above 1.0 Jy km s^{-1} (AVCs 1–3), we are left with 11 clumps in the 0.06–0.23 Jy km s^{-1} flux range. These are indicated in Figure 15.

Integrating the full empirical distribution leads to an expected mean of 4.1 false detections per masked data cube. With an algorithm flux detection threshold of 4σ, and for 177,500 independent samples in our masked data cube, we expect 5.3 detections of greater than 4σ significance from purely statistical considerations. That the simulations average fewer false detections indicate limitations of our detection algorithm. Both false detection rates are consistent with our "by-eye" analysis indicating that AVCs 9–14 are spurious. The chance of obtaining at least six spurious detections given the simulation mean of 4.1 is 22%; given the statistical mean of 5.3, the chance is 44%.

We note that the simulations do not account for systematic errors which may occur from bandpass calibration or continuum subtraction and which may introduce artifacts similar to clumps of emission. Some of our "detections" show indications of this effect (e.g., the multiple velocity components of AVCs 11 and 14). Excluding these, the number of false detections is still consistent with the expected rate. Modeling of systematic calibration errors will be included in future versions of the simulation software.

The completeness of our sample was determined from the detection efficiency, which in turn was found from additional simulations. Twenty data cubes with noise characteristics similar to the data were created in the manner described above. To each of them were added 200 three-dimensional Gaussian sources with spatial FWHM = 40″ (approximately the synthesized beamwidth), velocity FWHM = 5 channels (25 km s^{-1}), and peak brightness varying between 1.0 and 5.0 mJy/beam in steps of 0.5 mJy/beam. The integrated fluxes of the sources varied between 0.01 and 0.27 Jy km s^{-1}. The positions of the sources were produced semi-randomly so that the centers were not necessarily at integer pixels but the sources did not overlap within 5σ in any direction. The resulting cubes were processed with our detection software in an identical fashion as the source data.

At least 90% of the simulated sources were detected to a flux of 0.16 Jy km s^{-1}, as is shown in Figure 16. Below this, the detection efficiency falls off rapidly, reaching 50% at a flux of about 0.1 Jy km s^{-1}. The shape of the efficiency curve may explain the lack of low-flux detections in our sample. Also from these simulations, we note a systematic flux overestimate of $\sim$ 10% for a simulated 0.2 Jy km s^{-1} clump and $\sim$ 30% for 0.1 Jy km s^{-1}. The measured AVC fluxes have not been corrected for this effect.

6. DISCUSSION

Different HVC production scenarios predict different characteristics for the HVCs. The galactic fountain predicts that material will be projected on the disk, while tidal stripping and accretion predict HVCs across the field of view. We can divide the detected AVCs into two categories: those projected on the disk (AVCs 1, 2, and 4 and the low relative velocity extended emission), and those projected away from the disk. Separate treatment of each group places constraints on the importance of the various HVC formation schemes.

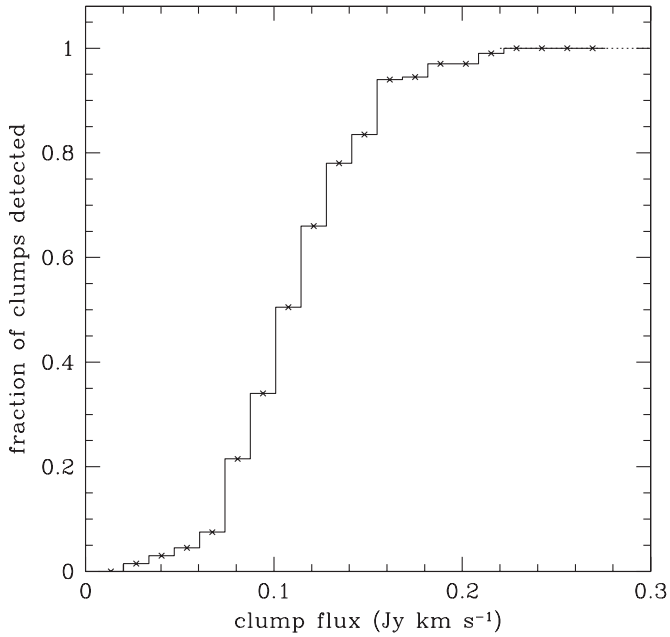

Figure 16. Detection efficiency of the simulated clumps. The efficiency is 90% above 0.15 Jy km s^{-1}.

6.1. Galactic Fountain: "The Beard" and HVCs

Under the galactic fountain model, hot gas is ejected from the disk by multiple supernova explosions in star-forming regions. This material rises at roughly the adiabatic sound speed, moves outward due to a decrease in the radial gravitational potential, and rotates more slowly due to conservation of angular momentum. After the gas cools, it loses its buoyancy and spirals back to the disk, either as small clouds or sheets (Shapiro & Field 1976; Bregman 1980).

The observational implications of this model depend in detail on the nature of the hot corona and magnetic field, which are ill-constrained, but several general features should be apparent in observations of external galaxies. First of all, discrete clouds of scale $\sim$ 1 kpc should be observable at velocities between systemic and systemic plus the coronal sound speed ($\lesssim$ 150 km s^{-1}), on both wings of the disk velocity profile. Second, H I emission could appear at velocities between systemic and the disk, i.e., on the low relative velocity wing of the disk profile. This emission could be spatially extended (spanning a few kpc) if small-scale condensations are suppressed (Field 1965; Mathews & Bregman 1978; Chevalier & Oegerle 1979; Bregman 1980). Finally, anomalous velocity H I should coincide with the spiral arms and Hα disk emission, especially the discrete high-velocity clumps, which would be infalling near their point of origin.

Our results are consistent with these predictions. The extended anomalous disk of H I appears to be rotating more slowly than the main H I disk, which would be the case for emission from a galactic fountain. This material must be spatially separated from the bulk H I, and we conclude that it lies in a vertically extended disk. A similar phenomenon has been observed in a number of inclined spiral galaxies, including NGC 891 (Swaters et al. 1997; Oosterloo et al. 2007), NGC 2403 (Fraternali et al. 2002b), NGC 4559 (Barbieri et al. 2005), NGC 253 (Boomsma et al. 2005), and NGC 6946 (Boomsma et al. 2008). In particular, for the $i = 60^\circ$ spiral NGC 2403, Fraternali et al. (2002b) argue that this emission, termed the "beard" due to its appearance in p–v diagrams, arises from a vertically extended H I component that is rotating 20–50 km s^{-1} more slowly than the cold disk. They model the anomalous disk and characterize it as having a radial inflow at velocity $\lesssim$ 20 km s^{-1}, implying an inflowing mass rate of $\dot{M} \sim$ 0.3–0.6 $M_\odot$ yr^{-1} for an infall timescale of $\sim 10^8$ yr. They also detect 10^6–10^7 $M_\odot$ "streams" and "spurs" of H I emission, ranging in size from 5–10 kpc and deviation velocity from 50–60 km s^{-1}. They conclude that this material arises from a galactic fountain, with a mass exchange rate close to the predicted value of $\sim$ 1 $M_\odot$ yr^{-1}. Further evidence is provided by *Chandra* X-ray observations showing an extended corona of $T \sim 5 \times 10^6$ K gas with a radiative cooling rate of 0.1–0.2 $M_\odot$ yr^{-1} (Fraternali et al. 2002a). Additional modeling by Fraternali & Binney (2006) supports this conclusion, although it suggests that some amount of IGM accretion must be present to temper the fountain and produce the low angular momentum material.

The face-on inclination of M 83 makes it difficult to model the rotation of the beard component in the same way as Fraternali et al. (2002b), Fraternali & Binney (2006), and others. It is also not clear whether the anomalous disk is radially infalling as is the case of NGC 2403, nor is it clear how vertically extended the material is. If the beard is the result of a galactic fountain, it is likely that it represents material near maximum z because of its low velocity, and it probably is gas that has recently condensed and is beginning to fall back onto the disk. The discrete clouds projected on the disk at higher deviation velocities would be in freefall at lower z. If the column density of a cloud exceeds that of the disk, the cloud would punch through and disrupt the H I disk in that location. AVC 3 is projected over a region of low disk $N_{\rm H\,I}$, however it is projected near the warp and not the spiral arms, so it may have a different origin than the other disk-coincident AVCs.

The dynamical properties of the AV gas are consistent with what would be expected in a galactic fountain. The beard mass of 5.6×10^7 $M_\odot$ (8.4×10^7 $M_\odot$ including the AVCs) and an estimated cooling/freefall time of 5×10^7 yr leads to a mass exchange rate of 1 $M_\odot yr^{-1}$, similar to the predictions of the model (Bregman 1980). The star formation rates of M 83 and the Milky Way are similar, so one would expect similar mass exchange rates. Talbot (1980) estimates a star formation rate (SFR) in the Milky Way between 1.7 $M_\odot$ yr^{-1} (from converting CO measurements to H_2) and 2.0 $M_\odot$ yr^{-1} (from Hα). Bell & Kennicutt (2001) constrain the SFR of M 83 to be between 1.1 and 2.4 $M_\odot$ yr^{-1} from FUV and Hα data, using the relations of Kennicutt (1998). The mass infall rates in both galaxies are estimated to be $\sim$ 1 $M_\odot$ yr^{-1}, consistent with the similar SFR. The kinetic energy of the discrete AVCs projected over the disk total about 7×10^{53} erg, equaling the total output of about 1000 supernovae. This is a lower limit to the kinetic energy initially imparted to the gas by the collection of supernovae, since the velocity is measured in only one direction and the z height of the AVCs is unknown. A supernova rate of 0.01 yr^{-1} is consistent with this if only 1% of the energy is converted to kinetic energy.

6.2. Galactic Disruption and Accretion: External HVCs

It is difficult to reconcile the presence of AVCs projected outside the stellar disk with the galactic fountain model, thus there is likely another HVC production scenario at work. AVCs 3, 7, and 8 are projected on the H I warp/ring, and are possibly associated with that. The remainder of the AVCs are compact, and all except AVCs 5 and 6 are likely spurious detections.

The optical results rule out emission from a population of dwarf galaxies similar to those in the Local Group. The 3σ

detection limits for the AVCs projected outside the H I disk are at least 26.8 r' magnitudes per square arcsec. Assuming an integrated color $V-R \sim 0.4$–0.6, typical of Local Group dwarfs (Mateo 1998), and using the SDSS filter transformation from Smith et al. (2002), this corresponds to about 27.2 V magnitudes per square arcsec. This limit is faint enough to detect the center of any of the dwarfs tabulated by Mateo (1998). Likewise, the inferred ratios of $M_{\rm H\,I}/L_V > 2M_\odot/L_\odot$ are larger than those of the majority of Local Group dwarfs, indicating a dearth of starlight compared to these systems.

Our optical depth is similar to that of other HVC studies. Willman et al. (2002) use SDSS data to search for stellar components in 13 Galactic HVCs, detecting none to limits of 26.7–30.1 V magnitudes per square arcsec. Simon et al. (2006) obtain an upper limit of 25.25–26.25 V magnitudes per square arcsec for HVC Complex H, depending on the assumed stellar population. Fainter companions and stellar streams are observed in the Milky Way and M 31, but they do not have evidence of H I emission (e.g., Zucker et al. 2004; Willman et al. 2005).

If they are real, these H I clouds are best explained by a combination of tidal disruption and accretion. The H I warp, H I ring, and elongated, gas-free companion KK208 are all evidence supporting a tidal interaction at some point in the galaxy's past. In addition, an unpublished wide-field H I map shows evidence of an H I arm to the N of the galaxy, extending east from the tip of the longest NW arm visible in Figure 3 (Park et al. 2001). Our field of view is insufficient to include this region, but it is further evidence of a tidal interaction that can strip diffuse material and produce anomalous H I emission.

6.3. Limits on the Mass Distribution of Galactic HVCs

Our results are sensitive enough to place constraints on the mass distribution of the HVC ensemble in M 83 and, by extension, the Milky Way. Because of the variable mass sensitivity across the field, we restrict our analysis to AVCs detected within the half-power beamwidth (HPBW) of the primary beam. We assume that the full distribution of M 83 HVCs falls within this region, which is a reasonable assumption if the vertical distance z is less than about 50 kpc (and $z \sin i \lesssim 17$ kpc or 15′). Only the eight confirmed detections lie within the primary HPBW, and we scale our estimates of the false detection rate to the reduced number of independent sightlines we are now sampling. Five of the eight detected clumps have masses in a region where the false detection rate is significant (greater than 0.1 detection expected per mass bin), while the remaining AVCs are much more massive and unlikely to be spurious. Assuming a Poisson distribution for false detections, and using the integrated false detection rate as the mean "background" expected for a mass bin, we determine the background-corrected mass distribution with 90% confidence limits. This is shown in Figure 17, using the tabulated data of Gehrels (1986) to calculate confidence limits for low number counts. We obtain upper limits above an HVC mass of $1.2 \times 10^6\ M_\odot$ and below a mass of $6 \times 10^5\ M_\odot$; below $4 \times 10^5\ M_\odot$, the completeness falls below 50%, so we have cut off the distribution at this point.

To draw conclusions about the Galactic HVC population, two simplifying assumptions must be made. First, we assume that the underlying HVC mass distributions are identical for the Milky Way and M 83. Second, we assume the Galactic HVCs are contained in a uniform spherical distribution about the Galactic center. While this is likely incorrect, it is a sensible choice given our lack of knowledge of their distances. The collection of Galactic HVCs across the whole sky has been cataloged by Wakker & van Woerden (1991), and excluding the Magellanic Stream and outer Galactic arm, we randomly assign distances drawn from the assumed distribution to the cataloged HVCs. The assigned distances and cataloged H I fluxes produce an estimate of the Galactic HVC mass distribution. This procedure was repeated 500 times to fill in the high-mass regions, and the resulting distribution was scaled to the number of HVCs in the catalog (560).

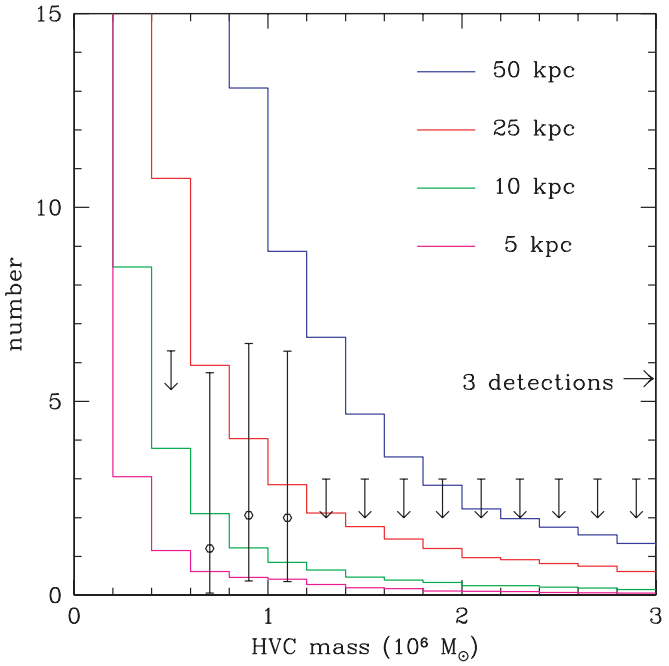

Figure 17. Mass distribution of the Milky Way HVCs, assuming uniform spherical distributions of varying mean distance and using the HVC catalog of Wakker & van Woerden (1991). The points show the distribution of our lowest-mass detections in M 83, with 95% confidence errorbars and upper limits. Three detections lie off the horizontal scale at $M_{\rm H\,I} > 5 \times 10^6\ M_\odot$. This distribution has been corrected for the false discovery rate (the "background") and the source detection efficiency. If the underlying HVC mass distributions of the two galaxies are identical, the Milky Way HVCs must be closer than about 25 kpc or we would have detected more HVCs in M 83.

(A color version of this figure is available in the online journal.)

The derived HVC mass distribution is plotted in Figure 17 for four different mean Galactic HVC distances, along with the HVC mass distribution for M 83. While the confidence limits are large, it is clear that an ensemble distance of less than about 25 kpc is consistent with the M 83 distribution, while a larger average distance results in a larger number of massive clouds. Such clouds would have been easily visible in our M 83 observations. It is possible that some HVCs in M 83 could fall outside the HPBW and therefore be missed if the distance is much greater than 50 kpc, however even at 50 kpc we detect an order of magnitude fewer HVCs than should be present in M 83. In addition, the heliocentric distances are upper limits to the more fundamental z height of the HVCs, therefore the distances of the HVCs from the plane are consistent with being less than about 10 kpc. Finally, if the HVCs cataloged by Wakker & van Woerden (1991) are not distinct but rather clumps within larger complexes, then the mass distribution derived here will underestimate the number of high-mass HVCs, and the constraints imposed by our results would be stronger.

These constraints are consistent with previous results. Wakker (2001) has published a catalog of 18 HVCs and 8 IVCs with distances and metallicities constrained by absorption against background stars or extragalactic sources. The metallicities

vary from solar to a few percent of solar. The upper bounds to the vertical z heights range from 0.1 kpc to 7 kpc, and the corresponding mass limits range from about 10^4 to 2×10^6 $M_\odot$. More recent results indicate distances of 5–15 kpc to a handful of additional Galactic HVCs (Thom et al. 2006; Wakker et al. 2007, 2008). Similarly, Putman et al. (2003) have detected Hα emission in 25 HVCs and use this to limit the distance of these objects from the ionizing Galactic radiation field and thus constrain their height above the Galactic plane. The values range from $5 < z < 40$ kpc. Limits from external galaxies are similar. Thilker et al. (2004) detected an ensemble of 20 discrete H I clouds within 50 kpc of M 31. These sources have H I masses in the range 10^5–10^7 $M_\odot$. A handful of the objects identified by these authors would be visible if present in M 83, and our results are consistent with this. Pisano et al. (2007) survey six analogs of the Local Group and detect no extragalactic H I emission. Using a similar analysis to ours, they conclude the Galactic HVCs must be distributed within 90 kpc and have average H I mass less than about $4 \times 10^5 M_\odot$. The handful of discrete HVCs we detect in M 83 could represent the high-mass tail of a much more abundant low mass, nearby population.

7. SUMMARY AND CONCLUSIONS

We have performed deep, wide-field imaging of the H I in M 83, mapping the outer features for the first time. The H I ring and warp seen by Tilanus & Allen (1993) are confirmed, and the outer arms extend to a radius of 34 kpc and show reflective symmetry, hinting at a tidal formation scenario. At least 80% of the H I mass is located outside the optical extent of the galaxy, with the possibility that more H I lies undetected outside the primary beam HPBW. The optical companion KK208 (Karachentseva & Karachentsev 1998; see Figure 5) contains no H I to a limiting column density of 1×10^{19} cm^{-2}.

We discovered a spatially-extended component of anomalous-velocity gas deviating 40–50 km s^{-1} from the bulk H I disk and coincident with it in projection, with a line-of-sight velocity dispersion of 10–15 km s^{-1}. We interpreted this as a vertically extended disk rotating in the same sense but about 100 km s^{-1} more slowly than the kinematically cold, thin disk. The 5.6×10^7 $M_\odot$ of H I it contains is 5.5% of the total H I within the stellar disk of the galaxy.

We have introduced a new technique of searching for faint extended radio emission, combining several existing tools and including statistically robust data modeling. Other recent studies have used similar techniques of contouring and extended source extraction (Putman et al. 2002; de Heij et al. 2002). These developments are driven by the need for lower detection limits in projects constraining the missing satellites problem and obtaining a full census of the Galactic HVCs.

Using this technique, our observations are sensitive to unresolved sources ($d \lesssim 1$ kpc) with masses greater than 5×10^5 $M_\odot$. We have discovered 14 discrete anomalous-velocity emission sources, of which we consider eight to be real detections, ranging in H I mass from 6×10^5 to 1.5×10^7 $M_\odot$ and projected on and off the disk. Three of these sources are high-significance detections and appear to be distinct H I clouds with masses in excess of 5×10^6 $M_\odot$. They are spatially extended and coincide in projection with the optical spiral arms. The flux distribution of the low-mass sources is inconsistent with purely spurious detections, therefore we conclude that most of these are real HVCs in the M 83 system. They are generally unresolved, off-disk features and are free of diffuse optical light to a limiting surface brightness of 27 r' mag per square arcsec.

We conclude that a combination of a galactic fountain and tidal stripping are responsible for the anomalous H I features that we observe in M 83. The handful of HVCs we have detected are likely to represent the high-mass end of a substantial HVC population in this galaxy. We expect future deep H I observations of nearby spirals to add to the growing number of HVC analogs detected in external galaxies, and to thereby shed light on the ubiquity of HVC activity and the nature of our own Galaxy's gaseous neighborhood.

We thank the staff of the VLA and CTIO for their assistance with the planning and execution of these observations. We especially thank Jonathan Williams and Juan Uson for providing access to and help with their source detection software code, and the anonmyous referee for constructive comments that improved the manuscript. E.D.M. would like to thank Mario Mateo, Hugh Aller, and Tim McKay for their helpful suggestions toward the improvement of this work.

APPENDIX

A NEW SOURCE DETECTION METHOD FOR SPECTRAL SYNTHESIS IMAGING

We have developed a suite of software that searches a spatially coherent, three-dimensional data cube for signal in a statistical way. This software borrows heavily from the methods and code developed by Uson et al. (1991) and Williams et al. (1994), but as we have made variations to the methods and translated much of the code to a new programming language, we here describe the new software in some detail.

The program begins by smoothing the input data cube in velocity with Gaussian kernels of the form

$$H(v) = e^{-(v^2/2\sigma_v^2)}, \tag{A1}$$

where σ_v is the width of the particular Gaussian. The convolution is performed by a fast Fourier transform. If one assumes a Gaussian velocity profile for a clump of emission, the signal due to this feature as a function of channel or frequency v would be

$$S(v) = A(v_0)e^{-(v-v_0)^2/2\sigma_{v,0}^2}, \tag{A2}$$

and the smoothing function acts as a matched filter, enhancing features of similar width and de-emphasizing narrower or wider features. In a given channel, the normalized amplitude of the smoothed feature is given by

$$\langle A(v_0)\rangle = \frac{\int S(v)H(v)\,dv}{\int H(v)^2\,dv}, \tag{A3}$$

where the integral is taken over the entire feature. This value is maximized when $\sigma_v = \sigma_{v,0}$. The normalization factor $1/\int H(v)^2 dv$ is such that the amplitude of the smoothed feature will equal the amplitude of the original feature under this same condition; otherwise, the smoothed amplitude will be depressed compared to the unsmoothed value.

One can calculate the significance level of such a detection by recognizing that the smoothed noise is

$$\langle \sigma(v_0)^2\rangle = \frac{\int \sigma_i(v)^2 H(v-v_0)^2 dv}{\left[\int H(v)^2 dv\right]^2}, \tag{A4}$$

if we assume that neighboring channels are independent and the noise (given as σ_i for channel i) sums in quadrature. The noise in

each channel is determined by reflecting the negative portion of the data histogram across the mean and performing an iterative 4σ rejection until the measured σ converges. The significance level is calculated as $\langle A(v_0)\rangle/\langle\sigma(v_0)^2\rangle^{1/2}$ and written to disk as a data cube.

Peaks in S/N are identified down to some detection threshold, typically around 4σ, with neighboring above-threshold pixels merged into groups. These three-dimensional groups or "islands" serve as kernels for an iterative contouring scheme, with successively lower thresholds applied to the S/N cube. Each group is extended by adding new pixels that are above threshold and share at least two corners with any member pixel. That is, only neighbors that share at least one dimensional plane with the member are added, so that neighbors at a diagonal in all three dimensions are excluded. The algorithm for this procedure is based on the CLUMPFIND software developed by Williams et al. (1994). The contours are produced in intervals (which only affect the processing speed) down to a specified level, typically 3σ, iterating at each level until no new neighbors are added to any groups and merging groups which meet the neighbor criterion. Finally, any immediate neighbors (i.e., sharing four corners or two parameter planes) above 1.5σ are added to each group to improve flux measurements. No merging or iterating is done at this point. Groups are eliminated if they contain fewer pixels than a completely unresolved source (10 pixels in our case), as these features are unphysical.

The group IDs are written to a data cube, which is applied to the original data cube as a mask for each group in turn. The total flux, centroid, and other parameters of the group are determined from the original data cube, using only the pixels that are members of the group. The primary beam correction is applied at this point, and the corrected flux and mass are recorded along with the uncorrected parameters.

REFERENCES

Barbieri, C. V., Fraternali, F., Oosterloo, T., Bertin, G., Boomsma, R., & Sancisi, R. 2005, A&A, 439, 947
Bell, E. F., & Kennicutt, R. C. 2001, ApJ, 548, 681
Bland-Hawthorn, J., & Maloney, P. R. 1997, Proc. Astron. Soc. Aust., 14, 59
Bland-Hawthorn, J., Veilleux, S., Cecil, G. N., Putman, M. E., Gibson, B. K., & Maloney, P. R. 1998, MNRAS, 299, 611
Blitz, L., Spergel, D. N., Teuben, P. J., Hartmann, D., & Burton, W. B. 1999, ApJ, 514, 818
Boomsma, R., Oosterloo, T. A., Fraternali, F., van der Hulst, J. M., & Sancisi, R. 2005, A&A, 431, 65
Boomsma, R., Oosterloo, T. A., Fraternali, F., van der Hulst, J. M., & Sancisi, R. 2008, A&A, 490, 555
Braun, R., & Burton, W. B. 1999, A&A, 341, 437
Bregman, J. N. 1980, ApJ, 236, 577
Bregman, J. N., & Harrington, J. P. 1986, ApJ, 309, 833
Briggs, D. S. 1995, PhD thesis, New Mexico Institute of Mining and Technology, Socorro, New Mexico
Chevalier, R. A., & Oegerle, W. R. 1979, ApJ, 227, 398
Clark, B. G. 1980, A&A, 89, 377
Comte, G. 1981, A&AS, 44, 441
de Heij, V., Braun, R., & Burton, W. B. 2002, A&A, 391, 159
de Vaucouleurs, G., de Vaucouleurs, A., Corwin, H. G., Buta, R. J., Paturel, G., & Fouque, P. 1991, Third Reference Catalogue of Bright Galaxies (New York: Springer-Verlag)
Field, G. B. 1965, ApJ, 142, 531
Fraternali, F., & Binney, J. J. 2006, MNRAS, 366, 449
Fraternali, F., & Binney, J. J. 2008, MNRAS, 386, 935
Fraternali, F., Cappi, M., Sancisi, R., & Oosterloo, T. 2002a, ApJ, 578, 109
Fraternali, F., van Moorsel, G., Sancisi, R., & Oosterloo, T. 2002b, AJ, 123, 3124
Gehrels, N. 1986, ApJ, 303, 336
Greisen, E. 1998, The AIPS Cookbook, National Radio Astronomy Observatory, http://www.cv.nrao.edu/aips/cook.html
Högbom, J. A. 1974, A&AS, 15, 417
Huchtmeier, W. K., & Bohnenstengel, H.-D. 1981, A&A, 100, 72
Kamphuis, J., & Briggs, F. 1992, A&A, 253, 335
Kamphuis, J., & Sancisi, R. 1993, A&A, 273, L31
Kamphuis, J., Sancisi, R., & van der Hulst, T. 1991, A&A, 244, L29
Karachentsev, I. D., et al. 2002, A&A, 385, 21
Karachentseva, V. E., & Karachentsev, I. D. 1998, A&AS, 127, 409
Kennicutt, R. C. 1998, ApJ, 498, 541
Klypin, A., Kravtsov, A. V., Valenzuela, O., & Prada, F. 1999, ApJ, 522, 82
Koribalski, B. S., et al. 2004, AJ, 128, 16
Landolt, A. U. 1992, AJ, 104, 340
Lockman, F. J. 2003, ApJ, 591, L33
Maller, A. H., & Bullock, J. S. 2004, MNRAS, 355, 694
Mateo, M. L. 1998, ARA&A, 36, 435
Mathews, W. G., & Bregman, J. N. 1978, ApJ, 224, 308
Mathewson, D. S., Cleary, M. N., & Murray, J. D. 1974, ApJ, 190, 291
Moore, B., Ghigna, S., Governato, F., Lake, G., Quinn, T., Stadel, J., & Tozzi, P. 1999, ApJ, 524, L19
Muller, C. A., Oort, J. H., & Raimond, E. 1963, C. R. Acad. Sci. Paris, 257, 1661
Oort, J. H. 1966, Bull. Astron. Inst. Netherlands, 18, 421
Oort, J. H. 1970, A&A, 7, 381
Oort, J. H. 1981, A&A, 94, 359
Oosterloo, T., Fraternali, F., & Sancisi, R. 2007, AJ, 134, 1019
Park, O.-K., Kalnajs, A., Freeman, K. C., Koribalski, B., Staveley-Smith, L., & Malin, D. F. 2001, in ASP Conf. Ser. 230, Galaxy Disks and Disk Galaxies (San Francisco, CA: ASP), 109
Pisano, D. J., Barnes, D. G., Gibson, B. K., Staveley-Smith, L., Freeman, K. C., & Kilborn, V. A. 2007, ApJ, 662, 959
Putman, M. E., et al. 2002, AJ, 123, 873
Putman, M. E., Bland-Hawthorn, J., Veilleux, S., Gibson, B. K., Freeman, K. C., & Maloney, P. R. 2003, ApJ, 597, 948
Putman, M. E., Thom, C., Gibson, B. K., & Staveley-Smith, L. 2004, ApJ, 603, L77
Sandage, A., & Tammann, G. A. 1987, Shapley-Ames Catalog of bright galaxies (2nd ed:, Washinton, DC: Carnegie Institution of Washington)
Schulman, E., Bregman, J. N., & Roberts, M. S. 1994, ApJ, 423, 180
Shapiro, P. R., & Field, G. B. 1976, ApJ, 205, 762
Simon, J. D., Blitz, L., Cole, A. A., Weinberg, M. D., & Cohen, M. 2006, ApJ, 640, 270
Smith, J. A., et al. 2002, AJ, 123, 2121
Sternberg, A., McKee, C. F., & Wolfire, M. G. 2002, ApJS, 143, 419
Stetson, P. B. 1987, PASP, 99, 191
Swaters, R. A., Sancisi, R., & van der Hulst, J. M. 1997, ApJ, 491, 140
Talbot, R. J. 1980, ApJ, 235, 821
Talbot, R. J., Jensen, E. B., & Dufour, R. J. 1979, ApJ, 229, 91
Thilker, D. A., Braun, R., Walterbos, R. A. M., Corbelli, E., Lockman, F. J., Murphy, E., & Maddalena, R. 2004, ApJ, 601, L39
Thom, C., Putman, M. E., Gibson, B. K., Christlieb, N., Flynn, C., Beers, T. C., Wilhelm, R., & Lee, Y. S. 2006, ApJ, 638, L97
Tilanus, R. P. J., & Allen, R. J. 1993, A&A, 274, 707
Tufte, S. L., Reynolds, R. J., & Haffner, L. M. 1998, ApJ, 504, 773
Uson, J. M., Bagri, D. S., & Cornwell, T. J. 1991, ApJ, 377, L65
van der Hulst, T., & Sancisi, R. 1988, AJ, 95, 1354
Wakker, B. P. 1991, A&A, 250, 499
Wakker, B. P. 2001, ApJS, 136, 463
Wakker, B. P., & Schwarz, U. J. 1988, A&A, 200, 312
Wakker, B. P., & van Woerden, H. 1991, A&A, 250, 509
Wakker, B. P., & van Woerden, H. 1997, ARA&A, 35, 217
Wakker, B. P., et al. 2007, ApJ, 670, L113
Wakker, B. P., et al. 2008, ApJ, 672, 298
Weiner, B. J., & Williams, T. B. 1996, AJ, 111, 1156
Williams, J. P., de Geus, E. J., & Blitz, L. 1994, ApJ, 428, 693
Willman, B., Dalcanton, J., Ivezić, Ž., Schneider, D. P., & York, D. G. 2002, AJ, 124, 2600
Willman, B., et al. 2005, ApJ, 626, L85
Zucker, D. B., et al. 2004, ApJ, 612, L121
Zwaan, M. A. 2001, MNRAS, 325, 1142